Radiation Measurements 180 (2025) 107329

Contents lists available at ScienceDirect

Radiation Measurements

journal homepage: www.elsevier.com/locate/radmeas

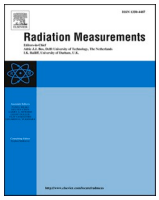

Monte Carlo dosimetry for a EURADOS WG 10 and RENEB field test of retrospective dosimetry techniques in realistic exposure scenarios

Hyoungtaek Kim [a,*], Min Chae Kim [a], Olivier Van Hoey [b], Jonathan Simon Eakins [c], Hyungjoon Yu [d], Hanjin Lee [d], Michael Discher [e], Jungil Lee [a], Lovisa Waldner [f], Clemens Woda [g,h], Francois Trompier [i], Céline Bassinet [i], Sergey Sholom [j], S.W.S. McKeever [j], Elizabeth A. Ainsbury [c]

[a] Radiation Safety Management Division, Korea Atomic Energy Research Institute, Daejeon, South Korea
[b] Nuclear Medical Applications Institute, Belgian Nuclear Research Center (SCK CEN), Mol, Belgium
[c] United Kingdom Health Security Agency (UKHSA), RCE, Chilton, Didcot, Oxon, UK
[d] Korea Institute of Nuclear Safety, Daejeon, South Korea
[e] Department of Environment and Biodiversity, Paris-Lodron University of Salzburg, Salzburg, Austria
[f] Department of Translational Medicine, Medical Radiation Physics, Lund University, Malmö, Sweden
[g] Institute of Radiation Medicine, Helmholtz Zentrum München, Neuherberg, Germany
[h] Federal Office for Radiation Protection (BfS), Oberschleißheim, Germany
[i] Institut de Radioprotection et de Sûreté Nucléaire (IRSN), F-92260, Fontenay-aux-Roses, France
[j] Department of Physics, Oklahoma State University, Stillwater, OK, USA

ARTICLE INFO

Keywords:
Reference dosimetry
Monte Carlo simulation
Computerized anthropomorphic phantom
Mesh and voxel type phantoms

ABSTRACT

Computational dosimetry using Monte Carlo radiation transport simulations was applied for the 2019 European Radiation Dosimetry Group (EURADOS) and Running the European Network of Biological and retrospective Physical dosimetry (RENEB) field test, an exercise of retrospective dosimetry techniques for a realistic small-scale radiological accident. The simulations were performed at four institutes, using different codes and computerized anthropomorphic phantoms. Four exposure scenarios using Ir-192 were modeled: relatively homogeneous in a predominantly AP direction, heterogeneous in a predominantly anterior-posterior (AP) and left-lateral (LLAT) direction, and partially shielded. The items for dosimetry, such as mobile phones, blood tubes, and surface dosimeters, were designed and located based on the experimental pictures. Absorbed doses of dosimeters, such as thermoluminescence dosimeter (TLD), optically stimulated luminescence dosimeters (OSLD), radio-photoluminescence dosimeters (RPLD), and display glasses, inside and outside the phantoms were calculated and compared to the measured doses. In addition, photon energy spectra were calculated at different locations to correct the energy responses of the materials. The simulation results from the four institutes showed agreement with each other, showing an average relative difference of less than 14%. The Pearson's R-values for the linear fitting of the measured and calculated data ranged from 0.95965 to 0.68714, depending on the exposure scenario and institutes. Finally, the accuracy and limitations of the calculation techniques for the given exposure structures are discussed.

1. Introduction

While the use of radionuclides and ionizing radiation have undeniably contributed to modern life, including nuclear energy, medical applications, industrial processes, and scientific discoveries, unfortunate accidents involving radiation have also occurred throughout history. Aside from well-known large-scale radiation accidents, such as the nuclear power plant failures in Chernobyl in 1986 (IAEA, 2006) and Fukushima in 2011 (IAEA, 2015), numerous small-scale radiation accidents have been documented (IAEA, 2024). Following each event, retrospective dosimetry techniques have been employed to estimate the radiation dose received by exposed individuals, facilitating appropriate medical interventions. For example, in December 2005, in Chile, a worker in a cellulose plant was exposed to a 3.33 TBq Ir-192 source

* Corresponding author.
E-mail address: kht84@kaeri.re.kr (H. Kim).

https://doi.org/10.1016/j.radmeas.2024.107329
Received 27 March 2024; Received in revised form 2 November 2024; Accepted 6 November 2024
Available online 9 November 2024

being used for industrial radiography. A whole-body dose of around 1.3 Gy was estimated using biological and physical dosimetry (Reyes et al., 2016), and a numerical dose reconstruction provided a 3D dose mapping of the patient's buttock as a guide for resection surgery of tissues that received a dose of over 20 Gy (Lataillade et al., 2007). In March 2006, in Belgium, an operator entered a cell in a high-dose irradiation facility and stayed there for a couple of seconds while a 30,000 TBq Co-60 source was stuck in the irradiation position. A whole-body dose of about 4.2 Gy was estimated using biological dosimetry, and 3.5 Gy was estimated by combining a numerical calculation with physical dose reconstructions (Huet et al., 2008). In March 2008, in Tunisia, a worker handled a 2.96 TBq Ir-192 source with his left hand for 10 min while manipulating a radiography camera. The whole-body dose was analyzed using biological and computational dosimetry, with similar results, between 0.25 and 0.28 Gy (Trompier et al., 2014). In June 2011, in Bulgaria, five workers were exposed to a 137 TBq Co-60 source, which was used for food sterilization, during a source recharging operation. The whole-body doses of the victims were estimated using biological dosimetry at two laboratories and ranged from 1.2 to 5.2 Gy with good agreement between institutes (Gregoire et al., 2013). In June 2012, in Peru, five persons were exposed to a 3.6 TBq Ir-192 source due to an operating failure during industrial radiography. EPR (electron paramagnetic resonance) and biological dose assessments of the most highly exposed victim showed a high inhomogeneity of the exposure, and Monte Carlo simulations using a mathematical phantom confirmed similar results (IAEA, 2018; Reyes et al., 2016; Trompier et al., 2014). Furthermore, in 2014, an incident occurred in Peru, where a worker was exposed to a 1.22 TBq Ir-192 source in close proximity to his skin as a result of malfunctioning industrial radiography equipment. Alongside other measurements, computational techniques were employed to identify specific areas on the skin that received absorbed doses exceeding the threshold for necrosis and to facilitate the development of an ablative treatment plan (IAEA, 2019).

As shown in these examples, retrospective dosimetry applies various methods, including biological, physical, and computational techniques, to improve exposure information. The biological dosimetry approaches analyze blood samples using well-established techniques, such as dicentric chromosome assay (DCA) and fluorescence in situ hybridization (FISH) (Kulka et al., 2018). Physical dosimetry employs the EPR technique for the fingernails, tooth enamels, and bones of a patient (Trompier et al., 2014; Williams et al., 2014). In recent years, physical measurements using thermoluminescence (TL) and optically stimulated luminescence (OSL) methods have been used on personal belongings such as electronic components and display glasses of mobile phones (Discher and Woda, 2013; Kim et al., 2019a; Sholom and McKeever, 2017). Numerical calculations using a computerized human body phantom can be used as powerful tools to estimate an absorbed dose for each organ and the entire body (Entine et al., 2022; Lemosquet et al., 2004). Also, using the Monte Carlo method has become an emerging technique for retrospective dosimetry, as more sophisticated and various structured anthropomorphic computerized phantoms are being developed (Hurtado et al., 2012; Kim et al., 2019b) and the computing power to simulate the complicated structure of phantoms has rapidly improved (Yeom et al., 2019).

International collaborations including both physical and biological dosimetry are actively underway. The RENEB network was built to perform retrospective dosimetry that is operational in large-scale radiological accidents. It also provides training, quality assurance for techniques, and networking with new methods (Kulka et al., 2017). The EURADOS working group (WG) 10 was established in recognition of the importance of integrating physical and biological dosimetry for the management of radiation accidents (Ainsbury et al., 2011). Inspired by these research networks, the Asian network for radiation dosimetry (ARADOS) (Kurihara et al., 2020) and Korean retrospective dosimetry (KREDOS) (Kim et al., 2022) were constructed by experts in Asian countries.

One of the main tasks of these research networks is to harmonize different techniques and evaluate the applicability of a multi-assay approach, which can be tested through inter-laboratory comparison (ILC). Regular ILCs are performed to harmonize existing techniques between institutions and to verify the feasibility of new methods. Studies are generally carried out in an individual laboratory by analyzing samples that have been irradiated in a standard radiation field (Ainsbury et al., 2017; Bassinet et al., 2014). Occasionally, field tests are performed to evaluate the applicability of dosimetry techniques by simulating virtual radiation accidents. For instance, a field experiment was conducted using various retrospective dosimetry techniques to estimate the doses to anthropomorphic phantoms after placing an Ir-192 source in the luggage compartment of a bus in an Austrian military area in 2014 (Discher et al., 2021a, 2021b; Rojas-Palma et al., 2020) as a re-creation of the Cochabamba incident in 2002 (IAEA, 2004), which provided the benchmark.

In October 2019, another field test was designed and conducted as a collaboration between EURADOS WG-10 and RENEB in Lund, Sweden (Waldner et al., 2021). The experiment simulated an accident in which several people were exposed to a highly active Ir-192 radionuclide source under different exposure conditions. The scenario was motivated by emerging concerns about radiation terrorism in public places, or a large-scale radiation accident leading to mass-casualties (Bailiff et al., 2016). In the experiment, more than thirteen institutes responsible for physical dosimetry were involved and all the biological laboratories in the RENEB network were included. First, blood samples located in vacuum flasks near the physical anthropomorphic phantoms during the exposure were analyzed using DCA and gene expression assays (Abend et al., 2021; Endesfelder et al., 2021). Second, the electronic components and display glasses in the mobile phones attached to the dummies were extracted, and measured by OSL and TL protocols (Woda et al, in preparation). Third, tooth enamel samples inside the mouths of the phantoms during the exposure were analyzed by EPR X-band spectroscopy. Fourth, additional fortuitous materials, including snacks, salt, cigarettes, chip cards, and textile bags were used to evaluate new protocols developed by individual labs. Finally, computational dosimetry was applied to verify the reliability of the technique and the validity of dose conversion (Eakins et al., 2024). The whole concept, purpose, and detailed methods of the experiment are well described in the first paper of the ILC (Waldner et al., 2021).

Since the field test was not carried out with a reference radiation field condition, reference dosimetry had to be performed to compare the doses of all samples. Reference dosimetry was carried out using OSLDs, TLDs, and RPLDs inside and outside the phantoms. Simultaneously, numerical calculations using the Monte Carlo method were conducted, taking into account the specific exposure geometry. Due to the lack of sophisticated measurements and recorded information that would be needed to reproduce the precise exposure conditions, these calculations aim not to provide accurate reference doses but to instead validate the calculation techniques using the resources available at the participating institutions, assuming the experiment was a real-world case with limited information. Therefore, the present study encompasses three main objectives. The first is to evaluate the reliability of calculation techniques by comparing them to reference measurements. To do that the doses absorbed by each reference material and the doses in organs of anthropomorphic phantoms were calculated and compared with the published experimental data. The second is to check for consistency in computational techniques by comparing results between participants who may have different interpretations and approaches. The results obtained by different institutes using MCNP6.2 (Werner et al., 2018) with the International Commission on Radiological Protection (ICRP) reference voxel phantoms (ICRP, 2009) and Geant4 (Agostinelli et al., 2003) with the ICRP reference mesh phantoms (ICRP, 2020) were compared as another ILC (Computational ILC). The third is to provide additional information to the other ILC groups. This included evaluating additional data such as energy spectra for dosimeter energy corrections,

doses at unmeasured locations, and the identification of measurement outliers. Consequently, the accuracy and limitations of the present calculation techniques for various exposure scenarios are discussed.

2. Materials and methods

2.1. Exposure condition and experimental setup

The experimental pictures are shown in Fig. 1 (a). Since a full description of the irradiation configurations is presented in the previous publication (Waldner et al., 2021), only the experimental setup related to the simulation as depicted in Fig. 1 (b) is dealt with in this section. An Ir-192 irradiator, commonly used in non-destructive testing (NDT) for industrial radiography (Tech-Ops 880 Sentinal), was used. The activity of the isotope was calculated to be 1.36 TBq on the day of the experiment. Although the source has a collimator providing a cone with an approximate opening angle of 60–90 degrees of an unshielded radiation field, anthropomorphic phantoms and all materials of interest were placed under the uncollimated area, which made it possible to assume

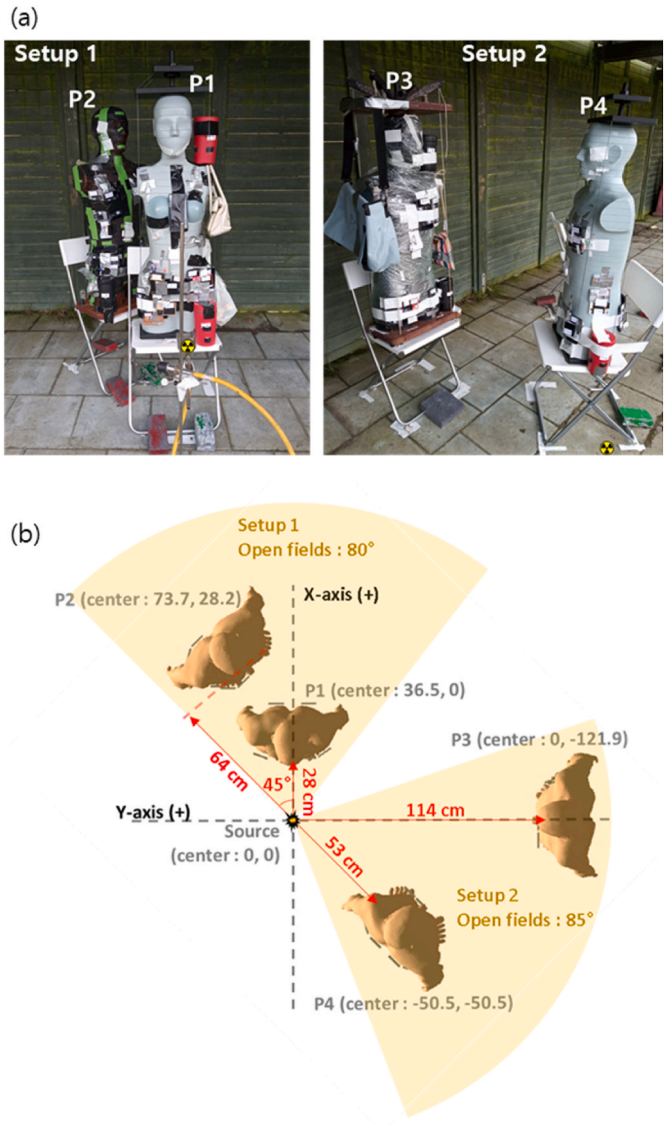

Fig. 1. The exposure geometry of setups 1 and 2: (a) photos of the field test and (b) a top view of the Geant4 simulation (created by combining the two exposure setups). In the simulation, the source is located at (0, 0) and the closest distances between the source and the surface of each phantom are given.

the exposure condition was irradiation from a point source. A total of four physical anthropomorphic torso phantoms were used to construct two different exposure setups, each consisting of two phantoms. All of the phantoms were placed on plastic chairs of the same size, with the bottoms of the phantoms about 46 cm away from the flat concrete floor. In both exposures, the Ir-192 source remained approximately 59.5 cm above the floor.

In the first exposure, designated setup 1, an adult female anthropomorphic torso phantom (ATOM 702, CIRS inc., VA) (P1), which is based on a height of 160 cm and weight of 55 kg female (CIRS, 2021), was placed facing the source to form a heterogeneous AP exposure geometry. The shortest distance between the surface of P1 and the isotope was approximately 28 cm. An adult male anthropomorphic torso phantom (Rando, Alderson Research Laboratories, USA) (P2), which is based on a height of 175 cm and weight of 73.5 kg male (RSD, 2021), was also positioned facing the source but placed behind P1's right shoulder at an angle of 45° degrees to P1, to achieve a partial shielding effect. The center of P2 was located 72 cm in the x-direction and 26.5 cm in the y-direction, where P1 was placed in the x-direction.

In the second exposure, designated setup 2, another adult male anthropomorphic torso phantom (Rando, Alderson Research Laboratories, USA) (P3), was installed so that the closest distance from the source to the surface of P3 was 114 cm, forming a relatively homogeneous AP exposure. The other adult male anthropomorphic torso phantom (model ATOM 701, CIRS Inc., VA) (P4), which is based on a height of 173 cm and weight of 73 kg male (CIRS, 2021), was placed so that the radionuclide source was located near its left side, forming a predominantly LLAT exposure. The distance between the left waist of P4 and the source was approximately 53 cm. Due to the 45° angle between directions from the source to phantoms P3 and P4, there was no overlap between P3 and P4 in terms of the radiation field. The irradiation times were 1 and 2.5 h for setup 1 and setup 2, respectively.

All of the materials of interest were attached inside and outside the phantoms. Reference dosimeters such as RPLDs (GD301 and GD351 model) (Chiyoda Technol Corp., Tokyo, Japan) and OSLDs made of NaCl (Waldner et al., 2020) were attached together on the upper left, upper right, center, lower left, and lower right of the front and rear of the torso of all phantoms to verify the surface dose distribution. Organ doses were also recorded by reference dosimeters inside the phantoms. P1 was filled with RPLDs which is the same type as above, P2 was filled with 309 LiF:Mg,Cu,P (MCP-N) TLDs (RADCARD Corp., Krakow, Poland), and P4 was filled with NaCl pellets which is the same type as above. There were no dosimeters inside P3. Moreover, two vacuum flasks containing human blood samples for DCA and gene expression assays were placed around the thigh and shoulder of each phantom as follows: the left thigh and left shoulder for P1, the left and right thigh for P2, the left thigh and left shoulder for P3, and the left and right thigh for P4. RPLDs were attached to each blood tube inside of the flask and were also placed on the top, bottom, front, back, left, and right sides of the flask to obtain reference doses for the biological dosimetry. In addition, various mobile phones containing fortuitous dosimeters, such as display glasses and resistors, were attached around the chest, thigh, and hip of each phantom. Thin-layer Al_2O_3:C OSLDs (LUXEL) (LANDAUER Corp., Illinois, USA), LiF:Mg,Cu,P TLDs (GR-200), and reference glasses were placed inside and outside the mobile phones to estimate reference values for the TL/OSL techniques. Here, the term reference glass refers to thermally annealed display glass extracted from a mobile phone. Lastly, tooth enamel pieces were placed inside the mouths of the phantoms, and additional fortuitous materials including snacks, salt packs, cigarettes, Kleenex, chip cards, textiles, and more were positioned around the phantoms with RPLDs of the same type as above.

2.2. Monte Carlo simulations

Monte Carlo dosimetry for the field test was carried out using the Geant4 code with the mesh-type reference computational phantom

(MRCP) (ICRP, 2020) and the MCNP6.2 code with the reference voxel phantom (ICRP, 2009). Four institutes, the Korea Atomic Energy Research Institute (KAERI), the United Kingdom Health Security Agency (UKHSA), the Belgian Nuclear Research Center (SCK-CEN), and the Korea Institute of Nuclear Safety (KINS), participated with different codes and phantoms. Each institute simulated a slightly different geometry without affecting the overall exposure scenario as shown in Table 1.

2.2.1. Geometry and dosimeter designs

The overall simulation structure is similar for all participants. Therefore, the modeling made in Lab 1 is first introduced in this Section, followed by detailed differences between each laboratory in Section 2.2.2.

In the simulation with the Geant4 (version 10.5.0) code, the deposited energies on all the materials and tissues were calculated using the G4PSEnergyDeposit class. The primary photons and the secondary electrons were all accounted for in the simulation. The results were presented as a dose per particle and converted into an absorbed dose by applying the corrections for the beam emission direction biasing and multiplying by parameters characterizing the exposure, namely, irradiation time, photon yield of the source, and activity of the source (1.36 TBq). The source was assumed to be a point source. Separate simulations were carried out for setups 1 and 2, and the number of primary photons was set to 10^9 for each exposure setup. Each phantom was placed in a standing posture without removing the arms and legs, and the surrounding environment was filled with air. All the phantoms were 46 cm away from the ground. Since the physical source was collimated toward the phantoms, the ground scattering was assumed to be ignored in the simulation. A beam biasing option was used to create radiation fields with 80° degree opening azimuth angle for setup 1 and 85° degrees for setup 2, covering both phantoms, respectively. The energy spectrum and yield of the Ir-192 isotope were obtained from the Nuclear Decay Data for Dosimetric Calculations contained in ICRP 107 (ICRP, 2008). An overlay of the cross-section in the source plane and a top view of the phantoms is shown in Fig. 1 (b).

P1 was modeled using the adult female MRCP with a height of 163 cm and a weight of 60 kg, and P2, P3, and P4 were modeled using the adult male MRCP with a height of 176 cm and a weight of 73 kg. Given the anatomical differences between the MRCPs and physical phantoms, such as the width and thickness of the torsos, it was decided to place the MRCPs based on the shortest distance between the source and the surface of the torsos rather than to align them with the center of the physical phantoms. This was required to use the front dosimeters as a reference point for comparison between measurements and calculations. Besides, since the physical phantom had no legs, the vertical position of the source was set relative to the head and scaled based on the height of the physical and computational phantoms. As a result, the source was placed around 80 cm and 90.5 cm from the bottom of the female and male MRCPs, respectively, which is the inguinal region for both phantoms.

The reference dosimeters used in the simulation are presented in Table 2. The measured organ doses were compared to those derived from the MRCPs. A custom-designed mobile phone structure, comprising a front touch glass, a display glass (6.72 x 13.86 × 0.04 cm^3), a resistor (1.7 x 9 × 0.035 cm^3), a battery, a printed circuit board (PCB), and a plastic cover, as described by Kim et al. (2019b), was employed. Given that the resistors and LUXEL OSL dosimeters share Al_2O_3 as their primary component (Kouroukla et al., 2014), the LUXEL dosimeter was not designed separately and the resistor dose was used. The other dosimeters were shaped as discs having a 25 mm radius and 0.8 mm thickness to increase the detection area and reduce statistical uncertainty. For the vacuum flask, the disc dosimeters were placed around a simple stainless steel cylinder (radius (outer) 4 cm, height (outside) 15 cm, thickness 0.1 cm) filled with water. Instead of placing RPLDs and blood tubes inside the cylinder, the absorbed dose to RPLDs in the blood tube was estimated by averaging the doses of the RPLDs surrounding the flask.

Based on the pictures taken during the experiment, the designed dosimeters were all placed around each MRCP as shown in Fig. 2. Exceptionally, the vacuum flasks, BLD-1 and BLD-2 on P4, were repositioned below the hands compared to their original locations. This adjustment was made to accommodate the intact (no limbs were removed) MRCP. The placement of RPLDs attached to the extra materials is discussed in Sec 3.2.4.

2.2.2. Differences in exposure design between institutes

The exposure geometry, encompassing the relative locations and arrangements of the physical phantoms in relation to the radiation source, as well as the experimental pictures, were shared with the four participants. Each laboratory conducted simulations based on their own interpretation of the provided information. Therefore, exposure geometry can be slightly different between the participants. Furthermore, some of the modeling differences that have arisen and may arise between institutions are as follows.

- The position of the radiation source was determined based on the body shape of the computerized phantoms, considering factors such as distance to the skin and height ratio. Consequently, slight differences in source position may arise between the voxel and mesh phantoms.
- With the exception of Lab 1, a disc-shaped dosimeter with a 25 mm radius, composed of multiple thin layers as previously described, was applied to represent mobile phones. Furthermore, in Lab 3, disc-shaped dosimeters were placed at the blood tube positions without incorporating a vacuum flask.
- For Lab 2 and Lab 3, electron tracking was not included, and therefore, calculations were conducted using the kerma approximation. (Charged-particle equilibrium was expected in all cases).
- The placement of dosimeters varied based on the judgment of the designers. Particularly, in Labs 2 and 3, when two mobile phones were adjacent, a single disc-shaped dosimeter was employed in certain locations.
- Due to computer memory issues, Lab 2 solely performed simulations for scenario 1 using a voxel phantom for P1, while P2 was simplified as a rectangular slab of water. Therefore, no doses were recorded by Lab 2 for P2, with its surrogate included just to provide backscatter for P1.
- Both Lab 2 and Lab 3 utilized torso phantoms by removing the limbs from the reference voxel phantoms to better mimic the actual experimental setup.

Table 1
Applied Monte Carlo codes and anthropomorphic phantoms according to the participants. The included dosimetry items are listed.

Participants	Code	Anthropomorphic phantom	Mobile phone	Surface dosimeter	Vacuum flask	Organ
Lab 1	Geant4	Ref. Mesh	Incl.	Incl.	Incl.	Incl.
Lab 2	MCNP6.2	Ref. Voxel[a]	Incl. (only P1)	–	–	Incl. (only P1)
Lab 3	MCNP6.2	Ref. Voxel[a]	Incl.	–	Incl.	Incl.
Lab 4	MCNP6.2	Ref. Voxel	–	–	–	Incl.
	Geant4	Ref. Mesh	–	–	–	Incl.

[a] The arms and legs of the phantoms were removed in these simulations to match the physical torso phantoms used in the field test.

Table 2
The composition and density of the materials defined in the Geant4 simulation, corresponding to the measured materials.

Target	Measured materials	Designed structure	Density (g/cm^3)	Composition (Atomic fraction (≥1) or weight fraction (%))
Organs	TLD (MCP-N)	Organs	See ICRP Publication 145 (ICRP, 2020)	
	OSLD (NaCl)			
	RPLD			
Mobile phones	OSLD (LUXEL)	Mobile phone (Kim et al., 2019c)	3.75	O(47.2%)Mg(0.6%)Al(50.8%)Si(1.4%)
	Ref. glass		2.54	O(48.5%)Na(0.7%)Mg(0.6%)Al(15.9%)Si(27.1%)Ca(7.2%)
	TLD (GR-200)	Disc	2.64	Li(1)F(1)
Surface dosimeters	OSLD (NaCl)		2.16	Na(1)Cl(1)
Vacuum flasks	RPLD		2.61	P(31.55%)O(51.16%)Na(11%)Al(6.12%)Ag(0.17%) (Benali et al. (2017))
Extra materials				

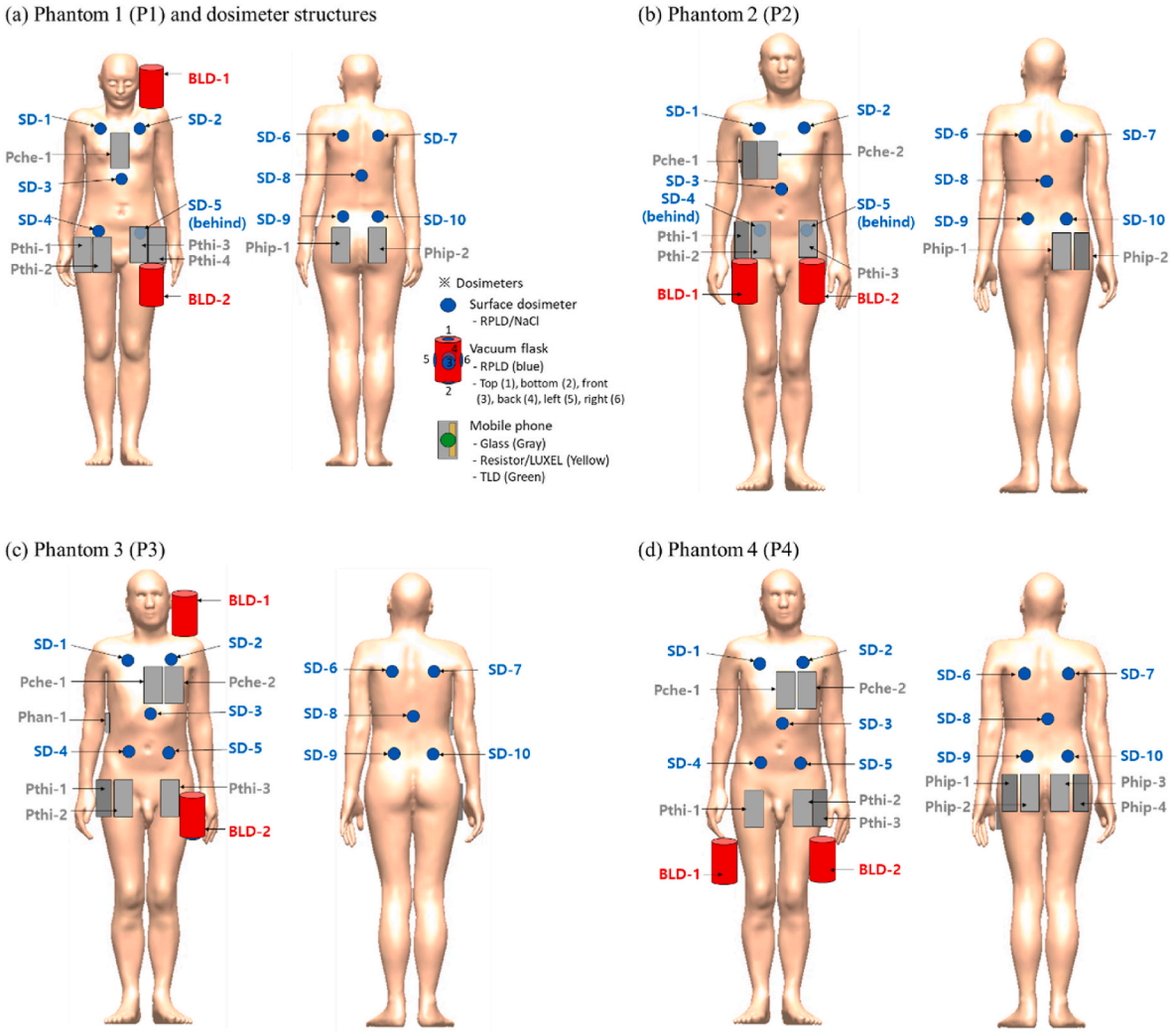

Fig. 2. The placement of the designed dosimeters on (a) P1, (b) P2, (c) P3, and (d) P4 based on the photographs taken during the field experiment. The dosimeter structures and corresponding materials are given in Fig. 2 (a). The surface dosimeters are named SD-1 to SD-10; if they are located behind a mobile phone, they are labeled as 'behind'. The mobile phones are named Pche, Pthi, Phip, and Phan depending on their position on the chest, thigh, hip, and hand (or shoulder bag), respectively. The vacuum flasks are marked BLD-1 and BLD-2. The RPLDs surrounding the flask are labeled as follows: 1 (top), 2 (bottom), 3 (front), 4 (back), 5 (left), and 6 (right), with the front RPLD oriented towards the source.

- Lab 4 conducted two simulations: Geant4 with mesh phantoms and MCNP6.2 with voxel phantoms. The dosimeters were not applied for these simulations. Electron tracking was implemented in the Geant4 code, while the MCNP6.2 code employed the kerma approximation.

In the present Monte Carlo calculations, the uncertainties resulting from the exposure geometry, the placement of the phantoms and dosimeters, and the dosimeter structures were not considered. The statistical uncertainties ($k = 1$) were determined to be less than 1% for most of the calculations because of the high number of primary photons in the

simulations. The error bar was omitted in the following plots unless it exceeded 3%, which was a circumstance that arose primarily in the smaller-sized organs.

2.2.3. Calculation of the photon energy spectra

The measured signals from the reference dosimeters were converted to dose quantities, such as air kerma (K_{air}) or absorbed dose to water (D_{water}), using a calibration procedure with standard radiation fields, including Co-60, Cs-137 sources, and high-energy x-rays from a linear accelerator (LINAC). However, the isotope source used in the field test emits photons with multiple energy levels, which deviate from the standard radiation fields. The energy spectrum of Ir-192 is known to range from several tens of keV to around 1 MeV, and the applied dosimeters have differing energy responses in the low-energy photon region. Additionally, the presence of anthropomorphic phantoms introduces shielding and backscattering effects that distort this energy spectrum depending on the position. Therefore, the Monte Carlo dosimetry task group needed to calculate the photon energy spectra in the organs and dosimeters to correct for energy response.

The G4VSensitiveDetector class was employed to record the kinetic energies of all incident photons at the surface of the detector. To have enough detection efficiency, photon energy detectors with a size of $10 \times 10 \times 1$ cm^3 and filled with air were placed in the corresponding positions of the surface dosimeters (SD-1 to SD-10). In addition, the organs of the MRCP were also used as detectors for the energy spectra. To avoid sharing repetitive and too detailed results, and to simplify the data reasonably, the spectra with similar distributions at nearby locations were averaged. Also, to estimate the energy spectrum, the photon energies were grouped into 10 keV energy bins, and the frequencies were normalized so that the total count sum equaled one.

2.2.4. Calculation of the whole-body dose

In computational retrospective dosimetry, several attempts have been made to assess the level of individual exposure by considering the whole-body dose (Eakins and Kouroukla, 2015) and the effective dose (Kim et al., 2019c). Therefore, two doses were calculated in this study as potential indicators of individual exposure. The whole-body dose was defined and calculated as the average of organ doses according to mass ratio. The effective dose was calculated by summing the organ doses, weighted by the ICRP 103 tissue weighting factors (ICRP, 2007). In ICRP 103, the weighting factors are sex-averaged values for reference adults, which may not be technically suitable for the specific female (P1) and male phantom (P2 - 4) employed.

2.3. Dose conversion

The measured doses of the reference dosimeters were acquired from the experimental studies (Endesfelder et al., 2021; Waldner et al., 2021; Woda et al, in preparation). The dosimeters that were attached inside and outside each mobile phone, i.e. reference glasses (thermally annealed display glasses), LUXEL OSLDs (Al_2O_3:C), and GR-200 TLDs (LiF:Mg,Cu,P), were measured at Helmholtz Zentrum München (HMGU), Oklahoma State University (OSU), and the Institut de Radioprotection et de Sûreté Nucléaire (IRSN), respectively. K_{air} was reported for each of these three dosimeters and a linear accelerator (LINAC, Elekta Synergy® Platform, 4 MV) at IRSN was used for calibration for each reference dosimeter under electronic equilibrium conditions. For RPLDs, placed inside of P1, on the phantom surface, in vacuum flasks, and on the extra materials, measurements were made at IRSN. Either K_{air} or D_{water} was reported depending on the location of the dosimeter. The calibration in terms of D_{water} was performed with the LINAC according to the specifications of the IAEA TRS-398 protocol (Musolino, 2001) and reference dosimetry was made using a PTW 31010 ionization chamber calibrated against Co-60 gamma rays. The calibration in terms of K_{air} was performed with a Cs-137 source at the IRSN reference facility. The LiF:Mg,Cu,P TLDs inside of P2 were evaluated at SCK-CEN, with K_{air} reported, using a Co-60 source for calibration. The Co-60 irradiation was performed at the vertical Co-60 gamma irradiator collimated with a 20° opening angle at the Laboratory for Nuclear Calibrations (LNK) Secondary Standard Dosimetry Laboratory at SCK CEN in terms of K_{air} according to the ISO 4037 standard under ISO 17025 accreditation by BELAC. The NaCl dosimeters inside of P4 were measured using an OSL protocol at Lund University, and the doses of the NaCl dosimeters placed on the phantom surface have not been reported yet. Measurement uncertainties were taken from the previous studies (Endesfelder et al., 2021; Waldner et al., 2021) and omitted if not available. The dosimeters used for measurement are summarized once again in the supplementary material (Table A1).

Each laboratory responsible for measuring the dosimeters within the organs reported their results as absorbed doses to tissue using the calculated energy spectra at the organs. The measurements of the other dosimeters outside of the phantoms were also converted to absorbed doses in the matter. In this calculation, the ratio of the mean mass energy-absorption coefficients was considered (Cunningham and Schulz, 1984; Furhang et al., 1995). In this approach, the air kerma from an energy spectrum (E), K_a, can be approximately converted into the corresponding absorbed dose to a specified material in that radiation field, D_m, as follows:

$$\mu_E \equiv \frac{D_m}{K_a} \tag{1}$$

$$\frac{D_m}{K_a} \approx \frac{\sum_i \left(\frac{\mu_{en}(E_i)}{\rho}\right)_m \bullet E_i \bullet \phi(E_i) \bullet \Delta E_i}{\sum_i \left(\frac{\mu_{en}(E_i)}{\rho}\right)_a \bullet E_i \bullet \phi(E_i) \bullet \Delta E_i} \tag{2}$$

where μ_E is the ratio of the mean mass energy-absorption coefficients for medium m and air. $\left(\frac{\mu_{en}(E_i)}{\rho}\right)_{m \text{ or } a}$ (cm^{2}g^{-1}) is the mass energy-absorption coefficient of medium m or air and $\phi(E_i)$ (keV^{-1}cm^{-2}) is the mean photon fluence (in air) within the i^{th} energy bin (E_i) with a bin width ΔE_i. The energy-dependent coefficients of the materials were obtained from the National Institute of Standards and Technology (NIST) database (Hubbell and Seltzer, 2004).

Furthermore, since the dosimeter calibrations were done in reference irradiation fields, the relative air kerma response at the energy spectrum (S_E) should be accounted for as follows (Hranitzky et al., 2006; Ixquiac-Cabrera et al., 2011):

$$S_E \equiv \frac{R_a}{K_a} \tag{3}$$

$$R_a = \frac{R_E}{R_{ref}} \cdot K_{ref} \tag{4}$$

$$\frac{R_a}{K_a} \approx \frac{\sum_i \left(\frac{\mu_{en}(E_i)}{\rho}\right)_a \bullet S(E_i) \bullet E_i \bullet \phi(E_i) \bullet \Delta E_i}{\sum_i \left(\frac{\mu_{en}(E_i)}{\rho}\right)_a \bullet E_i \bullet \phi(E_i) \bullet \Delta E_i} \tag{5}$$

where R_E and R_{ref} are experimentally measured dosimeter signals from the irradiation by the energy spectrum and the reference field, respectively, and K_{ref} is the air kerma at the reference field. $S(E_i)$ is the relative air kerma response at the i^{th} energy. The applied air kerma responses of different dosimeter materials were taken from the respective references: Display glass (Discher et al., 2014), TLD (LiF:Mg,Cu,P) (Parisi et al., 2019), OSLD (LUXEL, integrated signal stimulated for 300 s) (Gasparian et al., 2012), and RPLD (GD-301) (Weihai et al., 2007). It is worth mentioning that slight deviations in S_E may arise depending on the readout protocol and the detailed compositions of the materials (Gasparian et al., 2012; Parisi et al., 2019). Fig. 3 shows the relative air kerma responses and mass energy-absorption coefficient ratios for

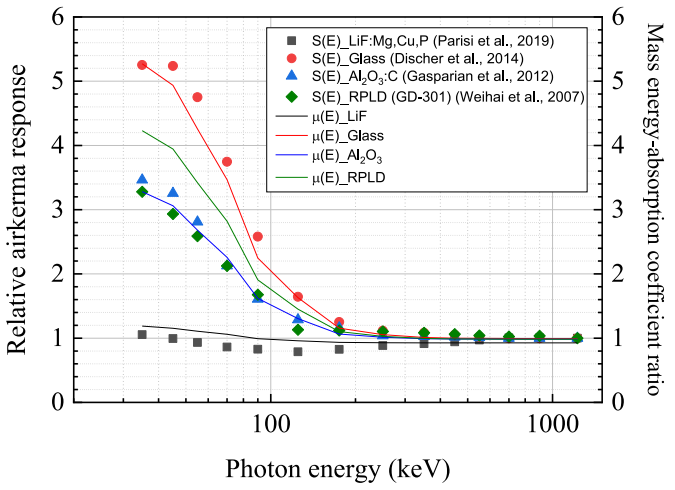

Fig. 3. Relative air kerma responses ($S(E)$) normalized to 662 keV (Cs-137) or 1220 keV (Co-60) and mass energy-absorption coefficient ratios ($\mu(E)$) for different dosimeters according to the photon energy: LiF:Mg,Cu,P (solid square and black line), Display glass (solid circle and red line), Al_2O_3:C (solid triangle and blue line), and RPLD (solid diamond and green line).

different dosimeters according to the photon energy. The reported measurement data were imported using Plot Digitizer and interpolated to the energies of the mass energy-absorption coefficients referred to in the NIST database (Hubbell and Seltzer, 2004). The chemical composition of the materials used to calculate the mass energy absorption coefficient ratios is presented in Table 2. For the RPLDs in the blood bottles, the mass energy-absorption coefficient ratios between RPLD and water were used, applying the relative D_{water} response (Benali and Ishak-Boushaki, 2018).

In Fig. 3, $S(E)$ and $\mu(E)$ exhibit similar energy-dependent behavior, leading to a canceling-out effect in dose conversion; the final values of these corrections are shown in the next section. Specifically, minimal conversion occurred in cases where both factors demonstrated a similar energy response, such as in Al_2O_3. However, slight discrepancies were observed in other dosimeters. For instance, TLD (LiF:Mg,Cu,P) exhibited a lower value of $\mu(E)$ (0.92) compared to $S(E)$ above 600 keV, while displaying a lower value of $S(E)$ below 200 keV, reaching as low as 0.8. Furthermore, below 100 keV, RPLD demonstrated a lower $S(E)$ by 25% compared to $\mu(E)$ and glasses present a higher $S(E)$ by 10% compared to $\mu(E)$. These deviations are consistent with previous studies (Benali and Ishak-Boushaki, 2018; Discher et al., 2014). It is worth noting that the uncertainty resulting from dose conversion was not considered due to limited available data on this matter and the minor impact of the conversion factors discussed later.

3. Results and discussions

3.1. Energy spectra and dose conversion coefficients

The photon energy spectra at the locations of the surface detectors and organs of the MRCPs were calculated. In Fig. 4, the spectra showing similar distributions were categorized and averaged depending on their positions. In the case of a predominantly AP exposure, P1 and P3, the photon fluence at the rear detectors become three times higher than that of the front detector below 100 keV, and the average photon energy is around 260 keV and 330 keV at the back and front, respectively. The largest energy spectrum shift occurred at positions SD-6, 8, and 9 of P2 with an average photon energy of 220 keV. The photon spectra for specific organs of P1, and for the entire phantom calculated by taking the arithmetic mean of the photon fluences for all organs, are depicted in the supplementary data (Figure A1). It can be seen that the spectra for the breast and brain, which are relatively free of surrounding materials, exhibit an average energy of about 300 keV, while those for the ovaries and adrenal glands are significantly affected by scattering.

Based on the energy spectra depicted in Fig. 4, correction factors were calculated for each dosimeter type using Eqs. (2) and (5), as presented in Table 3. The dose conversion was made by dividing the mean mass-energy absorption coefficient ratio by the relative air kerma response (μ_E/S_E). Given that the photon energy spectra on the back side of P2 were most significantly shifted towards lower energies, and that the materials exhibit different over-responses below 200 keV, the highest corrections, ranging from −6 to 3%, were required at SD-6, 8, and 9 of P2. The correction factors were applied to the dosimeters with corresponding positions, and it was assumed that the dosimeters at the

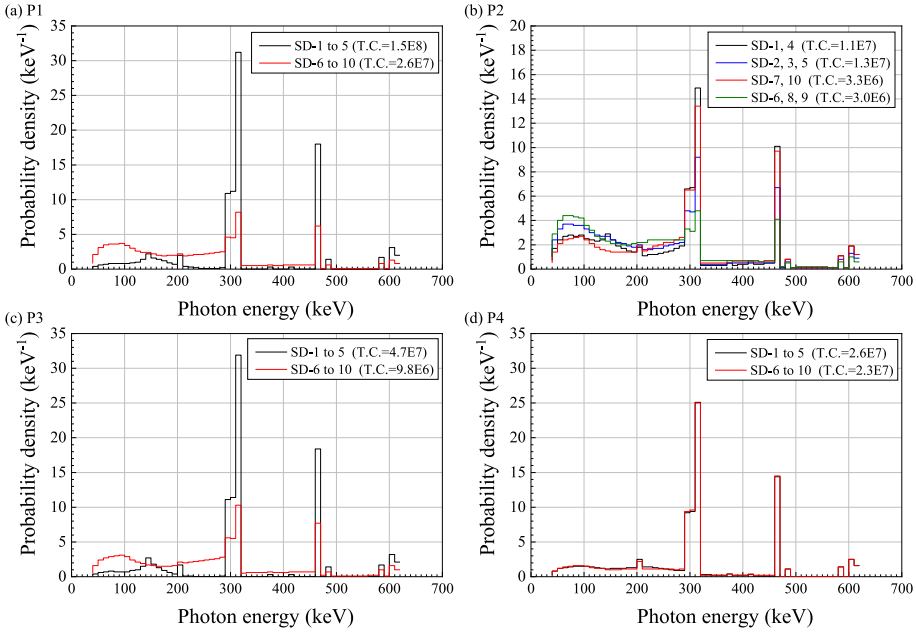

Fig. 4. Average probability density distribution of the incident photon energy at the position of the surface dosimeters (see Fig. 2) of each phantom. The legend shows the locations of the surface dosimeters used for the average and the corresponding total counts (T.C.) of the incident photons.

Table 3
Mean mass absorption coefficient ratios and relative air kerma responses calculated by Equations (2) and (5) according to the dosimeter materials and their positions in Fig. 2.

Dosimeter	Correction factors	P1		P2				P3		P4	
		SD-1 to 5	SD-6 to 10	SD-1, 4	SD-2, 3, 5	SD-7, 10	SD-6, 8, 9	SD-1 to 5	SD-6 to 10	SD-1 to 5	SD-6 to 10
TLD (GR-200)	μ_E	0.93	0.93	0.93	0.94	0.93	0.94	0.93	0.93	0.93	0.93
	S_E	0.94	0.92	0.93	0.92	0.93	0.91	0.94	0.92	0.93	0.93
	μ_E/S_E	0.99	1.02	1.01	1.02	1.00	1.03	0.99	1.01	1.00	1.00
Reference glass	μ_E	1.03	1.15	1.10	1.16	1.09	1.19	1.03	1.10	1.05	1.05
	S_E	1.08	1.21	1.16	1.22	1.15	1.26	1.08	1.17	1.10	1.10
	μ_E/S_E	0.95	0.95	0.95	0.95	0.95	0.94	0.95	0.95	0.95	0.95
OSLD (LUXEL)	μ_E	1.00	1.06	1.04	1.07	1.03	1.08	1.00	1.04	1.01	1.01
	S_E	1.03	1.09	1.07	1.10	1.06	1.11	1.03	1.07	1.04	1.04
	μ_E/S_E	0.97	0.97	0.97	0.97	0.97	0.97	0.97	0.97	0.97	0.97
RPLD (GD-301)	μ_E	1.01	1.10	1.07	1.10	1.05	1.13	1.01	1.07	1.03	1.03
	S_E	1.07	1.12	1.10	1.13	1.10	1.14	1.07	1.10	1.08	1.08
	μ_E/S_E	0.94	0.98	0.97	0.98	0.96	0.99	0.94	0.96	0.95	0.95

side positions of the phantoms (e.g. the left side of P4) had the photon energy spectrum equivalent to that on the front.

3.2. Comparison between the simulations and experimental data

Before we proceed with detailed comparisons, it should be mentioned that the present ILC study comprised two comparisons, the comparison between Monte Carlo calculations from the four institutes and the comparison with the reference dosimetry calibrated from the different laboratories. Since various doses are presented, for better understanding, the workflow for the correspondence between experiment and calculation is summarized in the supplementary material (Table A1). Moreover, certain degrees of discrepancy in the results are expected. First, there are inconsistencies between the actual exposure conditions and the computerized geometries due to the different choices made by each participant, all of whom had only limited information. Second, the anatomical gap between the physical torso phantom, the MRCPs, and voxel reference phantoms, introduces differences in shielding, organ doses, etc. Third, the measurements were provided by various institutes, potentially introducing systematic differences between them. To address a quantitative comparison of these discrepancies, i.e. the discrepancies between measured and calculated doses, and between calculated doses, a relative difference (RD) was introduced for each reference dosimeter as follows:

$$\mathrm{RD} = \frac{D_{sim} - D_{ref}}{D_{ref}} \tag{6}$$

where D_{sim} is the simulated dose and D_{ref} is the measured dose. If multiple reference dosimeters were used for measuring the dose to the target material, D_{ref} corresponds to their mean dose value. When a comparison was made within the computational techniques, i.e. the computational ILC for the organ doses, the RD was calculated by considering D_{ref} as the average of the doses to the target organ calculated by all participants. The RDs of each participant for the given exposure conditions and dosimeter groups are shown in Table 4. The data are averaged values for each item to represent the overall deviations. Note that the RD in the equation cannot be less than −1, while it can be much greater than +1. This asymmetry requires caution when analyzing data, as it can be misleading to think that the overestimate is much larger than the underestimate.

A comprehensive comparison based on materials regarding their energy response was not conducted, as the disparities between measurements and calculations were primarily attributed to different geometry. Instead, a meticulous assessment of the modeling's validity was carried out and is presented in subsequent sections, focusing on the items presented in Table 4. For the following plots and tables, terms are abbreviated as G(Lab1) for laboratory 1 with Geant4, M(Lab2) for laboratory 2 with MCNP6.2, and so on, unless stated otherwise.

Table 4
Average relative difference of each participant according to the exposure scenarios and target materials. The standard deviation for each value is provided. Simulations include Geant4 with MRCP of two laboratories (G(Lab1) and G(Lab4)), MCNP6.2 with a voxel reference phantom of three laboratories (M(Lab2*), M(Lab3*), M(Lab4)) (*simulated without limbs). The comparison within the calculation methods is only made for organs (Organs (cal.)).

		G(Lab1)	G(Lab4)	M (Lab2*)	M (Lab3*)	M(Lab4)
P1	Mobile phones	(12 ± 18)%	–	(41 ± 29)%	(39 ± 27)%	–
	Surface dosimeters	(29 ± 32)%	–	–	–	–
	Organs	(38 ± 111)%	(37 ± 110)%	(37 ± 117)%	(37 ± 116)%	(41 ± 115)%
	Organs (cal.)	(0 ± 8)%	(3 ± 6)%	(-3±8)%	(-2±7)%	(2 ± 6)%
P2	Mobile phones	(-17 ± 49)%	–	–	(32 ± 53)%	–
	Surface dosimeters	(11 ± 64)%	–	–	–	–
	Organs	(-56 ± 14)%	(-52 ± 12)%	–	(-41 ± 11)%	(-45 ± 14)%
	Organs (cal.)	(-11 ± 8)%	(-7 ±11)%	–	(14 ± 23)%	(6 ± 9)%
P3	Mobile phones	(8 ± 10)%	–	–	(15 ± 14)%	–
	Surface dosimeters	(23 ± 21)%	–	–	–	–
	Organs	–	–	–	–	–
	Organs (cal.)	(3 ± 4)%	(3 ± 6)%	–	(-10 ± 11)%	(3 ± 4)%
P4	Mobile phones	(13 ± 60)%	–	–	(59 ± 54)%	–
	Surface dosimeters	(11 ± 43)%	–	–	–	–
	Organs	(14 ± 23)%	(14 ± 22)%	–	(25 ± 34)%	(10 ± 23)%
	Organs (cal.)	(0 ± 6)%	(1 ± 6)%	–	(1 ± 18)%	(-2 ±7)%

3.2.1. Exposures in a predominantly AP direction

Fig. 5 shows the calculated doses obtained from the Geant4 and MCNP6.2 codes, as well as the measured doses of the dosimeters placed outside P1. In the case of mobile phones, the average RD between the calculations and the experiment was approximately 12% for the Geant4 code and 40% for the MCNP6.2 code. The higher deviation in MCNP6.2 is due to the use of different dosimeter positioning. Specifically, in the

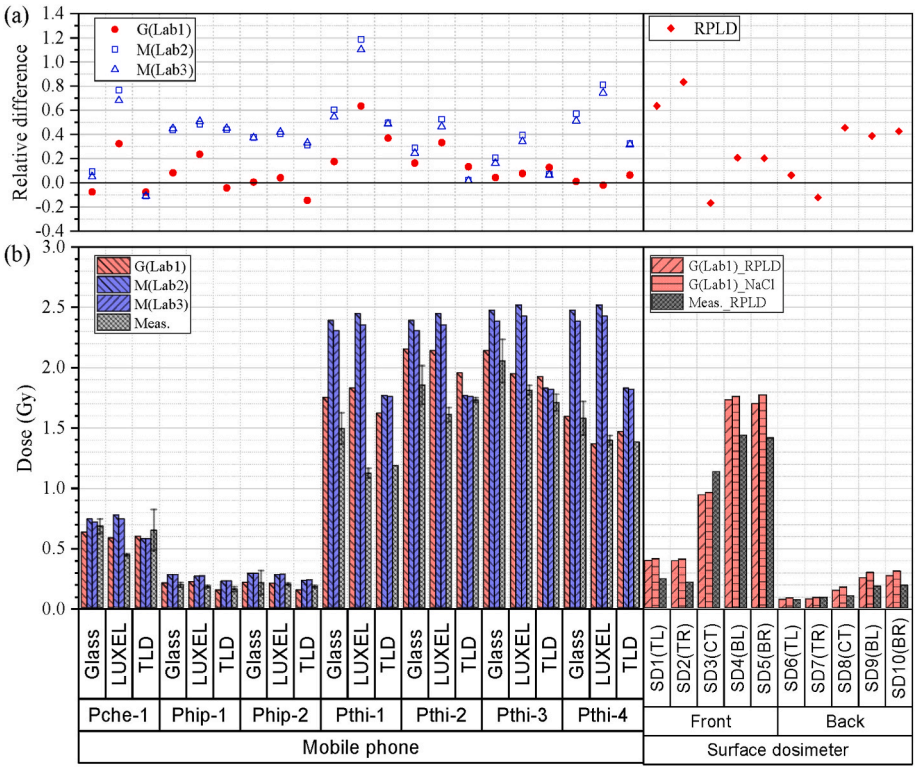

Fig. 5. Comparison of absorbed doses for the dosimeters on P1 according to the positions shown in Fig. 2, as estimated by Laboratory 1 with Geant4 (G(Lab1)) and Laboratories 2 and 3 with MCNP6.2 (M(Lab2) and M(Lab3)), and the measurements (Meas.). (a) Relative differences between the calculation and the measurement and (b) estimated doses are shown. For the surface dosimeters, the following positions are provided: top left (TL), top right (TR), center (CT), bottom left (BL), and bottom right (BR) of the torso. The measurement data were reproduced from (Waldner et al., 2021).

MCNP6.2 results, the doses for Pthi-2 and Pthi-4 were duplicated from Pthi-1 and Pthi-3, respectively, because a single dosimeter was modeled for the two adjacent physical dosimeters. Notably, positions Pthi-2 and Pthi-3 can be considered reference positions with a relatively well-defined distance between the source and the dosimeters. At these positions, the average RDs of Geant4 and MCNP6.2 were approx. 10% and 18%, respectively. Besides, both MCNP6.2 results exhibited similar doses, being within 5% of each other. In the case of surface dosimeters, the highest deviation was found at SD-2. In particular, considering that the source was located near the lower abdomen, the high deviations on the chest (SD-1 and 2) are presumed to be due to the different shielding effects resulting from the difference in breast shape and irradiation angle between the computational and physical phantoms. The back side also shows a deviation, but they are within −12% and 45%.

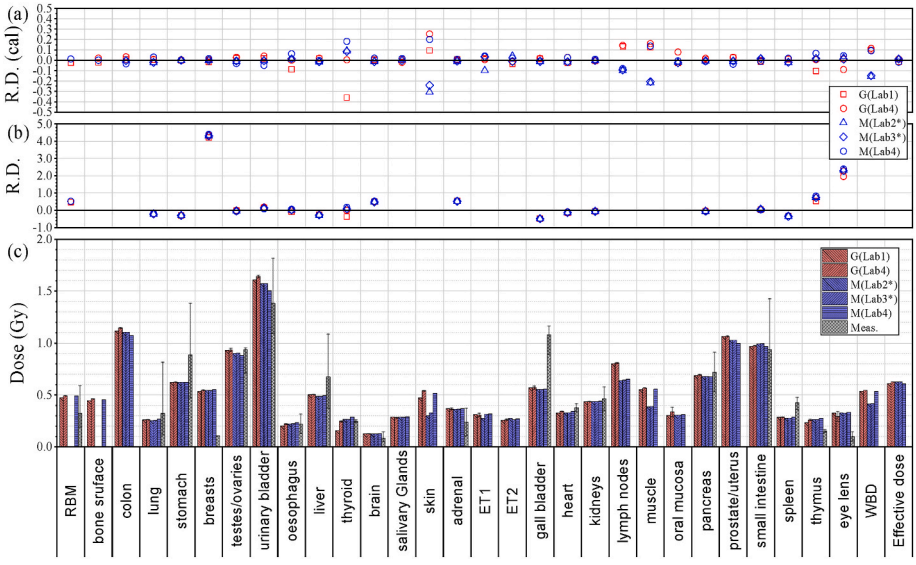

Fig. 6. Comparison of organ doses of P1, estimated by Geant4 with MRCP of two laboratories (G(Lab1) and G(Lab4)), MCNP6.2 with a voxel reference phantom of three laboratories (M(Lab2*), M(Lab3*), M(Lab4)), and measurements (Meas.). (a) Relative differences between the calculations, (b) relative differences between the calculations and the measurements, and (c) estimated doses are shown. The measurement data were reproduced from (Waldner et al., 2021). (* indicates without limbs).

The calculated and measured organ doses for P1 are presented in Fig. 6. First, in the computational ILC in Fig. 6 (a), the five participants produced almost similar values, being within ±10% of their average, except for some of the organs, including the thyroid, skin, lymph nodes, and muscles. It is clear that the presence of the arms and legs in some computerized phantoms (G(Lab1), G(Lab4), and M(Lab4)) caused the discrepancy in the absorbed dose in the skin, lymph nodes, and muscles compared to that of the others (M(Lab2), M(Lab3)). Also, the reduced absorbed dose in the thyroid of G(Lab1) was confirmed to be due to the additional shielding provided by the custom-designed mobile phone on the chest. Second, in Fig. 6 (b), a high consistency was found between the calculated and measured doses, except for some outliers. Especially in the breasts, gall bladder, thymus, and eye lens, significant over- and under-estimations were recorded. These outliers are considered the result of the anatomical differences of the anthropomorphic phantoms, such as organ size and locations. However, despite the large discrepancies between the real and computerized exposures, all participants produced doses with an average RD of less than 7% when excluding the two highest outliers (breasts and eye lenses).

The relatively homogeneous exposure of P3 is more intuitive than the other scenarios and makes the comparison much simpler. All average RDs of P3 in Table 4 show a close agreement between the calculated and measured doses when the standard deviations are taken into account. As shown in Fig. 7, the calculated data for the front-side dosimeters exhibit a systematic overestimation, with an average RD of approx. 8–15% depending on the participants. However, at the Pthi-2 and Pthi-3 positions, where the distance from the source is relatively well-defined, G(Lab1) and M(Lab3) showed average RDs of 4% and 10%, respectively. At the Phan-1 position, which was designated for a phone position in a hand or shoulder bag, no corresponding measurement was available. While SD-1 and SD-2 were expected to have similar doses due to the symmetry in the exposure, the measured data showed a lower dose at SD-2, resulting in up to 50% discrepancy at that point. This behavior is even the opposite of the result where the dose for SD-2 is calculated to be slightly higher than SD-1 due to the scattering from P4. Moreover, a high deviation in RDs is observed on the backside, presumably due to the differences in body thickness between physical and computational phantoms.

As mentioned, detailed dose comparisons according to the materials are challenging due to differences in exposure conditions between the experiment and the modeling. However, under homogeneous exposures such as P3, a partial analysis is possible. For M(Lab3), which used the identical disc shape structure for all dosimeters, the calculated dose of the TLD was found to be ~20% lower than that of the glass and LUXEL dosimeters at the same location. The lower TLD doses can be accounted for by two factors. Firstly, ~15% of the photons incident on the front dosimeters are below 200 keV, where the response of the other dosimeters increases. Secondly, at the 300 keV region, i.e. the main energy peak of the spectrum, TLDs exhibit a 7% lower mass-energy absorption coefficient compared to the other materials. On the other hand, a different behavior was observed in the measurements. Similar doses were measured between the LUXEL dosimeters and TLDs, while the glasses exhibited 10–20% higher doses than the other dosimeters. This resulted in higher RDs for the LUXEL dosimeters compared to the other dosimeters at the same position. Moreover, for the RPLDs attached to the front, a systematic overestimation by ~27% was observed in the calculations. These material-dependent discrepancies are not fully understood but may be due to differences in the material composition in the modeling or systematic errors occurring during the measurements.

Since the organ doses of P3 were not measured due to limited resources during the field test, only the four Monto Carlo simulations were conducted, as shown in Fig. 8. As also confirmed in the P1 case, the major source of the deviations in the computational ILC is the existence of the limbs. Excluding specific organs such as skin, lymph nodes, muscles, oral mucosa, and prostate, the RDs are found to be within ±10% for all calculations. The prostate dose in M(Lab3) being 15%

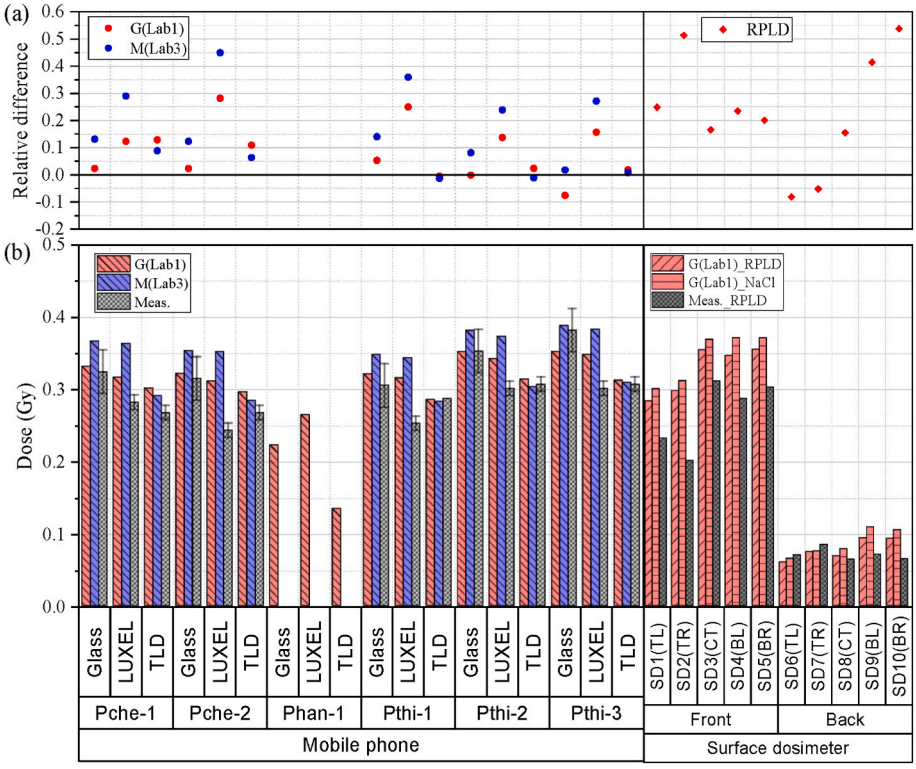

Fig. 7. Comparison of absorbed doses for the dosimeters on P3 according to the positions shown in Fig. 2, as estimated by Laboratory 1 with Geant4 (G(Lab1)) and Laboratory 3 with MCNP6.2 (M(Lab3)), and the measurements (Meas.). (a) Relative differences between the calculation and the measurement and (b) estimated doses are shown. The measurement data were reproduced from (Waldner et al., 2021).

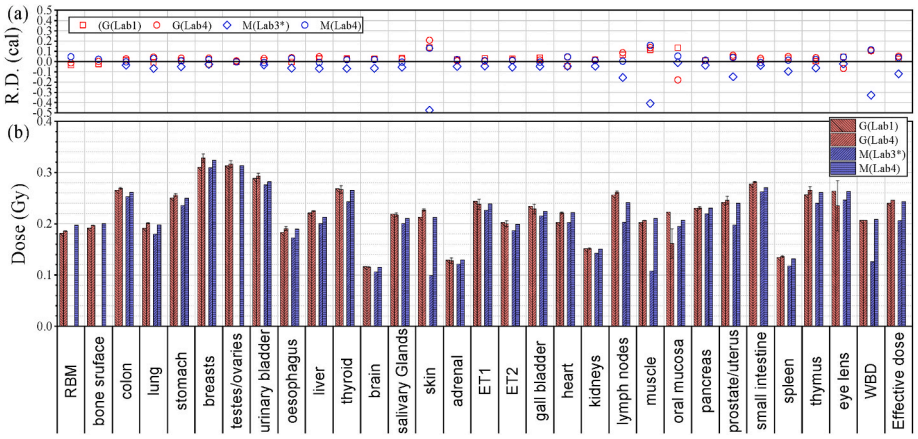

Fig. 8. Comparison of organ doses of P3, estimated using Geant4 with MRCP by two laboratories (G(Lab1) and G(Lab4)), and using MCNP6.2 with a voxel reference phantom by two laboratories (M(Lab3*), M(Lab4)). (a) Relative differences between the calculations, and (b) estimated doses are shown. The measurement data were reproduced from (Waldner et al., 2021). (* indicates without limbs).

lower than that of other participants is due to that organ being partially cut off during the leg amputation. For the same reason, the testes doses from all male phantoms of M(Lab3) were omitted.

3.2.2. *Exposures in partially shielded and a predominantly LLAT direction*

The dose assessment for the partially shielded P2 was the most unpredictable case in the field test since the exposure distribution was highly affected by P1. In Fig. 9, the estimated doses of the dosimeters placed outside P2 are shown. For M(Lab3), doses were duplicated between adjacent mobile phone positions, such as the right chest (Pche-1 and Pche-2), right thigh (Pthi-1 and Pthi-2), and right hip (Phip-1 and Phip-2). In most calculations, significant discrepancies were observed, particularly for the mobile phones on the front right side of the phantom. The dose distribution in this area can vary considerably depending on the shielding effect of P1. Specifically, the effect caused by the right arm of P1 is pronounced when comparing simulations with and without arms. At positions Pche-1, Pche-2, and Pthi-2, the calculated doses of G (Lab1) are approximately half of those of M(Lab3), indicating attenuation by the arm of the MRCP. Conversely, at the positions outside of the shielding area such as Phip-2, Pthi-1, and Pthi-3, the doses are similar between the two codes. The comparison with the experimental data further complicates the analysis. At Pche-1 and 2, the experimental data align more closely with the calculations simulated without the arms. However, at Pthi-1 and 2, the measured doses exceed the calculations by roughly a factor of two, which suggests less shielding by P1 during the experiment. Possible causes of these underestimations include the

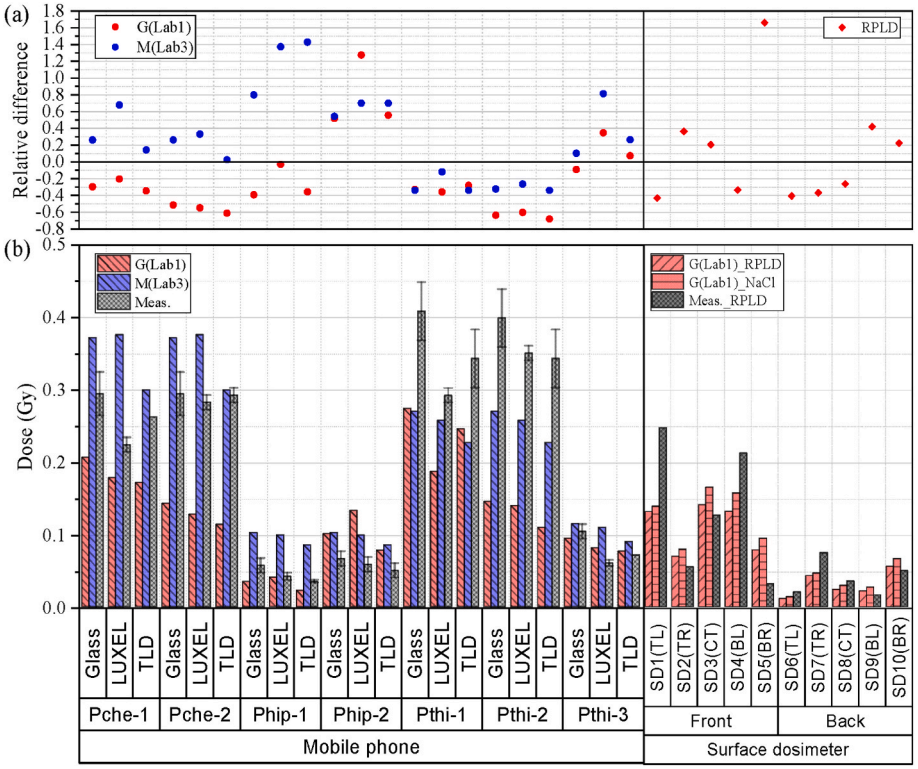

Fig. 9. Comparison of absorbed doses for the dosimeters on P2 according to the positions shown in Fig. 2, as estimated by Laboratory 1 with Geant4 (G(Lab1)) and Laboratory 3 with MCNP6.2 (M(Lab3)), and the measurements (Meas.). (a) Relative differences between the calculation and the measurement and (b) estimated doses are shown. The measurement data were reproduced from (Waldner et al., 2021).

inaccurate positioning of P2 and the different waist shapes of P1 in the modeling. Furthermore, the dose gradient behind P2 is still prominent in the measurements, resulting in the highest variations at Phip-1. Similar behavior is observed for the RPLDs as with the mobile phone doses in G (Lab1). The measured dose at SD-5 (30 mGy), which shows the highest RD, is considered an outlier since both the measured and simulated doses of the mobile phone materials at nearby positions (i.e., Pthi-3) ranged only from 60 to 110 mGy.

In Fig. 10, the estimated organ doses of P2 are compared. In Fig. 10 (a), significant deviations are observed between the calculations. Most results using the intact phantoms were found to be lower than those of the deformed torso phantom due to the additional shielding provided by the right arm of P1. On the other hand, the doses to the skin and muscles in M(Lab3) were lower than the others due to the absence of the limbs. The deviations among the three simulations using the intact phantom, namely G(Lab1), G(Lab4), and M(Lab4), resulted in an average RD ranging from −11% to 6%. On the other hand, most of the calculated organ doses were underestimated by approximately −50% compared to the measured doses, as shown in Fig. 10 (b). This underestimation, although reduced, is also observed in M(Lab3), indicating that the presence of the limbs alone cannot account for the discrepancy. Rather, it is attributed to limitations in interpreting and modeling partial shielding scenarios, stemming from uncertainties in phantom arrangement and anatomical differences. These limitations are further supported by the measurement data, which exhibit high error bars in Fig. 10 (c).

P4 was located in a highly heterogeneous exposure in a predominantly LLAT direction. In Fig. 11, a strong dose gradient is observed along the mobile phones located on the hip and thigh. The mobile phones at the Phip-4 and Pthi-2 positions were identified in the photographs, but no corresponding measurements were available. Again, doses of M(Lab3) were duplicated between adjacent mobile phone positions, such as the left chest (Pche-1 and Pche-2), left thigh (Pthi-2 and Pthi-3), left hip (Phip-1 and Phip-2), and right hip (Phip-3 and Phip-4). This approach exhibits doses that are close to the measurements at some positions, such as Pche-2, Phip-1, Phip-3, and Pthi-1, but it also introduced the highest deviations (up to 180%) at the positions near the source, such as Phip-2. In the case of G(Lab1), the calculated doses on the hips were underestimated by around −30%, whereas those on the thighs were overestimated by up to 190%. The opposite behavior between the front and backside suggests that the source of G(Lab1) was moved slightly closer to the anterior of P4 compared to the experiment. The discrepancy of the source location was also confirmed when comparing the doses at Pthi-1, as the doses of G(Lab1) were about 2 times higher than M(Lab3) despite the additional shielding effect from the left arm. This kind of inconsistency can be pronounced in a lateral exposure scenario since the center position relevant to a lateral exposure is ambiguous depending on the body shape of the computerized phantoms. A trend similar to the mobile phones is observed for the surface dosimeters. Most of the calculated doses on the front are overestimated by up to 90%, while those on the back are underestimated by up to −50%. Due to the cancellation effect, the average RD is 11 ± 43%.

When comparing the calculated organ doses in Fig. 12 (a), it can be observed that M(Lab3) exhibits relatively higher deviations (up to ±35%) compared to the others. Conversely, G(Lab1), G(Lab4), and M (Lab4) show deviations from each other of less than ±7%. The discrepancies observed in M(Lab3) are mainly due to the presence of the limbs. However, discrepancies are still observed in the doses to the brain and oral mucosa, which are not affected by the shielding effect of the arms, suggesting that M(Lab3) and the other participants have different source locations. In Fig. 12 (b), the calculated organ doses demonstrate an agreement with the measurements, with the average RDs ranging from 12% to 26% for all participants. However, notable overestimations of organ doses, exceeding 60%, were observed for the adrenal, kidneys, small intestine, and spleen, particularly in the case of M(Lab3). These discrepancies can be attributed to several factors, including differences in relative source positions, organ sizes, and organ locations between the computerized and physical phantoms.

3.2.3. Blood samples

The absorbed doses of the RPLDs inside and outside the vacuum flasks are compared in Table 5. The measured doses inside the flasks are the average of the median doses of the RPLDs attached to several blood tubes inside (Endesfelder et al., 2021). The calculated doses of G(Lab1) inside the flask are an average of the six RPLDs outside of the flask, assuming that the dose inside the flask is approximated to the surface dose that surrounds the whole face. The bottle IDs used in the biological dosimetry group are given. Although a degree of difference is observed between the measurement and simulations, the measured dose at the top of P1A is considered to be an outlier. The measured value of 0.32 Gy is

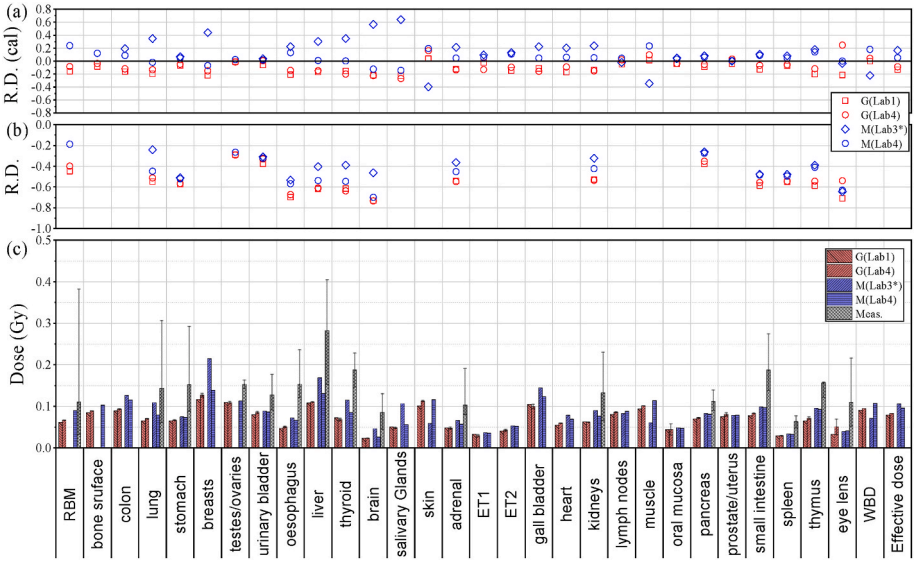

Fig. 10. Comparison of organ doses of P2, estimated using Geant4 with MRCP by two laboratories (G(Lab1) and G(Lab4)), and using MCNP6.2 with a voxel reference phantom by two laboratories (M(Lab3*), M(Lab4)), and measurements (Meas.). (a) Relative differences between the calculations, (b) relative differences between the calculations and the measurements, and (c) estimated doses are shown. The measurement data were reproduced from (Waldner et al., 2021). (* indicates without limbs).

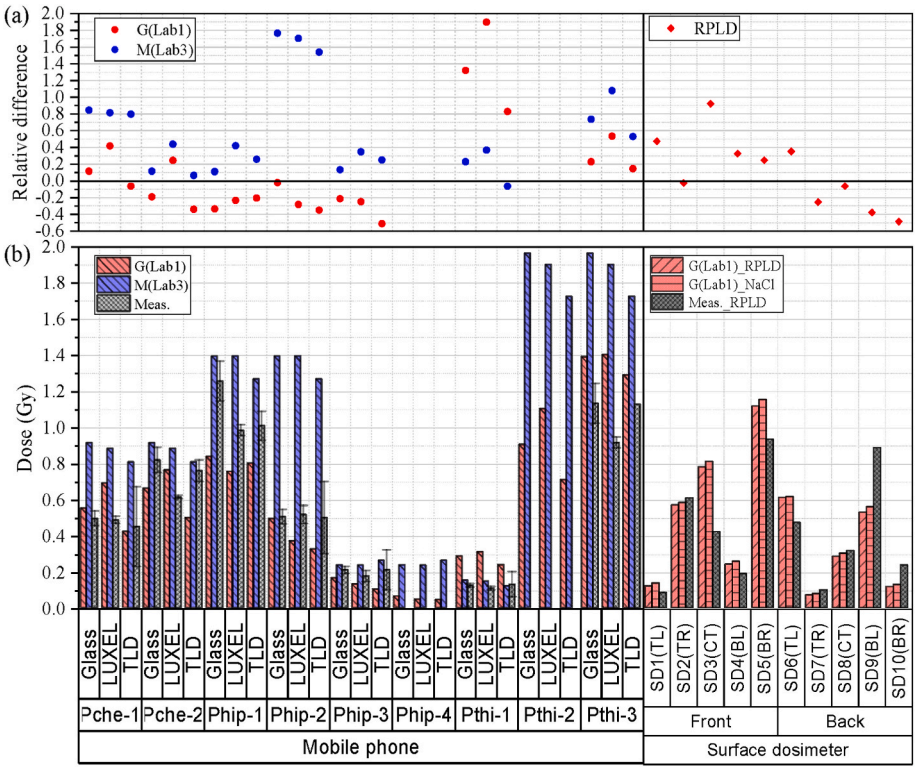

Fig. 11. Comparison of absorbed doses for the dosimeters on P4 according to the positions shown in Fig. 2, as estimated by Laboratory 1 with Geant4 (G(Lab1)) and Laboratory 3 with MCNP6.2 (M(Lab3)), and the measurements (Meas.). (a) Relative differences between the calculation and the measurement and (b) estimated doses are shown. The measurement data were reproduced from (Waldner et al., 2021).

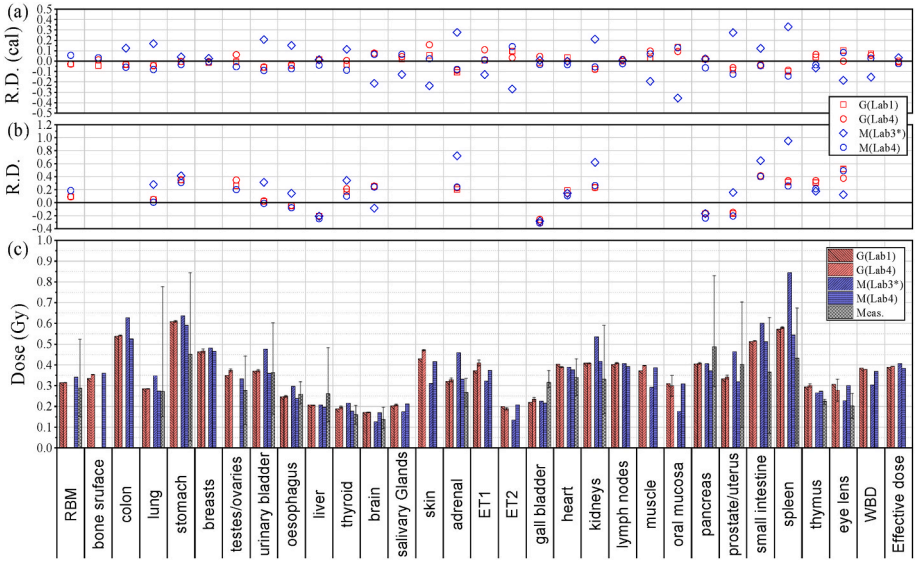

Fig. 12. Comparison of organ doses of P4, estimated using Geant4 with MRCP by two laboratories (G(Lab1) and G(Lab4)), and using MCNP6.2 with a voxel reference phantom by two laboratories (M(Lab3*), M(Lab4)), and measurements (Meas.). (a) Relative differences between the calculations, (b) relative differences between the calculations and the measurements, and (c) estimated doses are shown. The measurement data were reproduced from (Waldner et al., 2021). (* indicates without limbs).

significantly underestimated compared to the calculated dose range of 0.89–2.58 Gy around the bottle. Moreover, the dose assessed at Pthi-4, which is in a similar position to the top of P1A (BLD-2) in Fig. 2, is greater than 1.3 Gy in both calculations and measurements. The RDs inside of the flasks were found to be −4%–43% in G(Lab1) and −34%–119% in M(Lab3) showing a closer and narrower range when the custom-designed vacuum flask model was applied. It should be mentioned again that the vacuum flasks of P4 were shifted down from their original position due to the presence of the arms of the MRCP. Therefore, the underestimations at P4A and P4B were around −15% in the Geant4 calculation.

3.2.4. Additional data

The calculations for the extra materials are provided in the

Table 5
Comparison of absorbed doses for the RPLDs inside and outside the vacuum flasks in Fig. 2, as estimated from Geant4, MCNP6.2, and the measurements. Relative differences of the calculation to the measurement are given in the bottom rows. The measurement data are reproduced from (Endesfelder et al., 2021). (Dose unit: Gy).

Positions		Method	P1		P2		P3		P4	
			P1A (BLD-2)	P1B (BLD-1)	P2A (BLD-1)	P2B (BLD-2)	P3A (BLD-2)	P3B (BLD-1)	P4A (BLD-2)	P4B (BLD-1)
Surface	Top	Meas.	0.32	–	–	–	–	–	–	–
		G(Lab1)	1.80	0.11	0.31	0.09	0.22	0.15	1.62	0.04
	Bottom	Meas.	2.33	–	–	–	–	–	–	–
		G(Lab1)	1.32	0.17	0.29	0.08	0.18	0.27	0.84	0.03
	Front	Meas.	–	0.18	0.49	–	0.30	0.20	1.74	–
		G(Lab1)	2.50	0.28	0.48	0.13	0.32	0.25	1.54	0.06
	Back	Meas.	0.90	–	0.28	–	0.20	–	–	–
		G(Lab1)	1.18	0.07	0.26	0.06	0.18	0.12	0.71	0.02
	Left	Meas.	2.05	0.22	0.52	–	0.31	–	1.58	–
		G(Lab1)	2.58	0.28	0.30	0.09	0.33	0.24	1.12	0.06
	Right	Meas.	1.76	0.10	0.36	–	0.29	–	–	–
		G(Lab1)	0.89	0.15	0.44	0.12	0.24	0.18	1.14	0.03
Inside	Blood tubes	Meas.	1.78	0.12	0.36	0.10	0.28	0.17	1.37	0.05
		G(Lab1)	1.71	0.18	0.35	0.10	0.25	0.20	1.16	0.04
		M(lab3)	1.53	0.27	0.24	0.12	0.33	0.24	3.00	0.08
	Relative difference	G(Lab1)	−4%	43%	−5%	−2%	−13%	21%	−15%	−15%
		M(lab3)	−14%	119%	−34%	23%	17%	43%	119%	70%

supplementary materials. Table A2 presents the calculated absorbed doses in the teeth of the four phantoms, performed by Laboratory 3 using MCNP6.2. As there is no reported EPR measurement using tooth enamel, only the calculated values are included in this study. The whole-body doses and effective doses, calculated by different participants, are summarized in Table A3. In the absence of limbs, the whole-body doses were consistently underestimated by −28% to −38% compared to the intact phantoms, while the effective doses showed similar results between the participants. Table A4 presents the absorbed doses of the RPLDs attached to the extra materials. The dosimeter IDs indicate their positions as shown in Figure A2. Although the measurement data for dosimeter Ex-833 was lost, the simulation was able to provide the corresponding dose. The RDs varied from −58% to 61%, with an average of approximately 7 ± 29%.

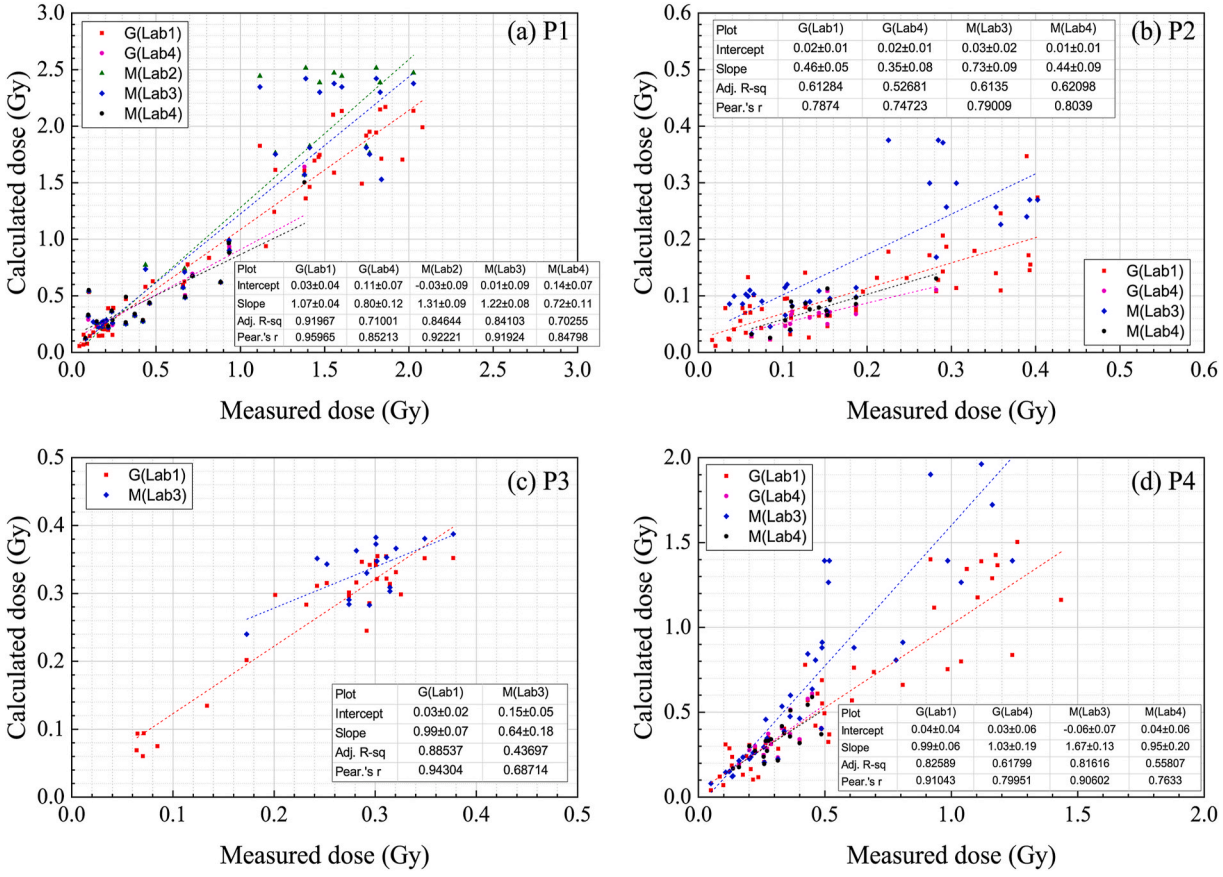

Fig. 13. Linear fitting of calculated doses to the measurements of (a) P1, (b) P2, (c) P3, and (d) P4, as estimated from the two laboratories with Geant4 (G(Lab1), G(Lab4)) and three laboratories with MCNP6.2 (M(Lab2), M(Lab3), M(Lab4)). The parameters(, such as the intercept, slope, adjusted R-square, and Pearson's R are shown in the inset.

3.3. Statistical analysis

Based on the previous results in Section 3.2, it was concluded that the accuracy in the computational simulation varied significantly depending on the exposure scenarios. To further analyze the overall agreement between the simulation results and corresponding measurements, a scenario-specific comparison with a statistical approach was performed and presented in Fig. 13. Linear fitting was applied using the built-in function in the Origin 2018 program, and parameters such as the slope, intercept, adjusted R-square, and Pearson's R values were evaluated. Unlike the overall deviations presented in Table 4, the evaluation of linear functions allows for the identification of under or overestimations in specific dose regions. For instance, although the average RDs of G(Lab4) and M(Lab4) at P1 are positive in Table 4, their linear fitting lines exhibit opposite behavior above 500 mGy in Fig. 13 (a). Pearson's R indicates the strength of the linear relationship between the measured and calculated data. Ranging between −1 and 1, a value closer to 1 signifies a stronger positive linear correlation. Additionally, adjusted R-squared provides a measure of how well the linear model fits the data. Falling between 0 and 1, a higher R-squared value indicates that the fitting line accounts for a greater proportion of the variability in the response data around the mean.

In Fig. 13 (a), it can be observed that G(Lab1) using the MRCP demonstrates the most linear and highly correlated results (See the high adjusted R-squared and Pearson's R). M(Lab2) and M(Lab3) showed 20–30% overestimation in the slope but still exhibited data correlation with Pearson's R greater than 0.9. About 20–30% underestimation in the slopes and the relatively lower adjusted R-squared values for G(Lab4) and M(Lab4) can be attributed to the inclusion of only organ doses, which have higher discrepancies compared to other dosimeters outside of the phantom. Overall, the most favorable statistical results were obtained for P1 compared to the other exposure scenarios. In Fig. 13 (b), consistent with the findings in Table 4, strong underestimations by 30∼65% in the slope are observed in all the fitting lines. Among the participants, M(Lab3), which modeled the torso phantom, demonstrates relatively better linearity. However, all adjusted R-squared values ranging from 0.52 to 0.62 indicate that most participants experienced the highest discrepancies in the presence of the partial shielding structure. In Fig. 13 (c), only dosimeters placed outside of the phantoms are included. As a result of the more uniform exposure of P3, both simulations exhibit similar data scatter above 200 mGy. However, the inclusion of additional data below 200 mGy in G(Lab1), such as the RPLD doses at the back and the extra materials, leads to improved linearity compared to M(Lab3). Forcing the intercept to zero in linear fitting is worth considering, but since the measured dose may differ from the true dose, it is difficult to conclude that the ideal calculated dose for a measured dose of zero should indeed be zero. Nevertheless, if the relatively high intercept value of the linear function of M(Lab3) for P3 is set to zero, the adjusted R-squared and Pearson's R are highly improved to 0.98693 and 0.99383, respectively. In Fig. 13 (d), G(Lab1) and M(Lab3) also demonstrate a high linearity and data correlation in terms of adjusted R-squared and Pearson's R values even with the presence of the limb-related issue. On the other hand, the higher slope observed in M(Lab3) indicates that the duplication of doses for this highly heterogeneous exposure resulted in systematic errors. Data from both G(Lab4) and M(Lab4) were fitted with a linear function having a slope of 1.03 and 0.95, respectively, but it is evident from the low adjusted R-squared values that the dataset exhibits high variation, primarily due to the organ doses.

3.4. Discussion

The comparison between the computational methods for organ doses showed meaningful results. Under relatively well-defined radiation exposure conditions such as P1 and P3, the difference between the two types of phantoms (MRCPs and reference voxel phantoms) was less than ±10% except for the organs relevant to the limbs. Larger deviations occurred when the arrangement of the source and phantoms was unclear under inhomogeneous exposures such as P2 and P4, and the presence of the limbs added significant variations. For instance, the dose variation between the intact phantom calculations in P2 was roughly ±20%, and it reached from −40% to 60% when the deformed phantoms were involved. When the dosimeter modeling is compared, there was little difference in doses between the fully designed mobile phone and the disc-shaped dosimeter, but the blood doses using the custom-designed vacuum flask produced more reliable results.

When comparing the calculations with the experimental data, a high consistency is observed overall showing Pearson's R-value up to 0.95965, demonstrating the reliability of the computational techniques in the ILC. However, significant outliers were confirmed in some positions on P2 and P4, which were mainly attributed to the discrepancies in the exposure geometry. Furthermore, the placement of the dosimeters introduced a high discrepancy when they were close to the source. This implies that the computational techniques need to be applied carefully in real scenarios where the precise exposure geometry is unknown. Analogously, the organ doses showed higher deviations between the calculations and measurements than the external dosimeters due to the anatomical differences of organs depending on the phantoms. These differences should be addressed in terms of uncertainty. However, the present calculations only give small statistical uncertainty ranges of less than a few percent. Therefore, in further studies, it is worth discussing the uncertainty estimation related to the uncertainty originated by the exposure geometry. For example, numerous calculations can be made with different source locations (Discher et al., 2021a), dosimeter placements, and different sizes of phantoms.

Lastly, the Monte Carlo simulations provided additional and comprehensive information in the field test. The calculation of the energy spectra allowed a reasonable approach for the absorbed dose conversion. The entire exposure distribution was reconstructed, enabling the estimation of doses at unmeasured locations and the identification of potential measurement outliers. Besides, it is possible to assess the effective dose for long-term risk, as well as whole-body doses for short-term risk management.

4. Conclusions

The Monte Carlo dosimetry was successfully performed in the EURADOS-RENEB 2019 ILC. The four exposure scenarios representing realistic radiological accidents were modeled and simulated with various dosimeters. Detailed analyses of the discrepancies and statistical evaluation according to the exposure scenarios were performed. As a result, the reliability and harmonization between the participants were evaluated quantitatively. Also, the limitations and major considerations of the applied techniques were addressed. The highest deviation was raised by the uncertainty of the exposure geometry. Therefore, further studies need to focus on a methodology of uncertainty estimation derived from an exposure geometry to apply dedicated simulations to possible radiological accidents.

CRediT authorship contribution statement

Hyoungtaek Kim: Writing – review & editing, Writing – original draft, Visualization, Validation, Supervision, Software, Methodology, Investigation, Formal analysis, Data curation, Conceptualization. **Min Chae Kim:** Visualization, Software, Methodology, Investigation, Conceptualization. **Olivier Van Hoey:** Writing – review & editing, Software, Methodology, Investigation, Conceptualization. **Jonathan Simon Eakins:** Writing – review & editing, Supervision, Software, Methodology, Investigation, Conceptualization. **Hyungjoon Yu:** Software, Methodology, Investigation, Conceptualization. **Hanjin Lee:** Software, Investigation. **Michael Discher:** Methodology,

Conceptualization. **Jungil Lee:** Investigation, Conceptualization. **Lovisa Waldner:** Investigation, Conceptualization. **Clemens Woda:** Writing – review & editing, Investigation, Conceptualization. **Francois Trompier:** Investigation, Conceptualization. **Céline Bassinet:** Writing – review & editing, Investigation, Conceptualization. **Sergey Sholom:** Investigation, Conceptualization. **S.W.S. McKeever:** Writing – review & editing, Investigation, Conceptualization. **Elizabeth A. Ainsbury:** Project administration, Investigation, Conceptualization.

Declaration of competing interest

The authors declare the following financial interests/personal relationships which may be considered as potential competing interests: Hyoungtaek Kim reports financial support was provided by Korea Ministry of Science and ICT. If there are other authors, they declare that they have no known competing financial interests or personal relationships that could have appeared to influence the work reported in this paper.

Acknowledgments

The study was carried out under the National Research Foundation of Korea (NRF) grant funded by the Korea government (Ministry of Science and ICT) (RS-2022-00144350, RS-2022-00144210) and Korea Atomic Energy Research Institute (project number: 521410-23). The international cooperation was conducted within task group 10.8 in the European Radiation Dosimetry Group (EURADOS) WG-10. The authors are grateful for the support of that group, especially those involved with setting-up the ILC and those who contributed data.

Appendix

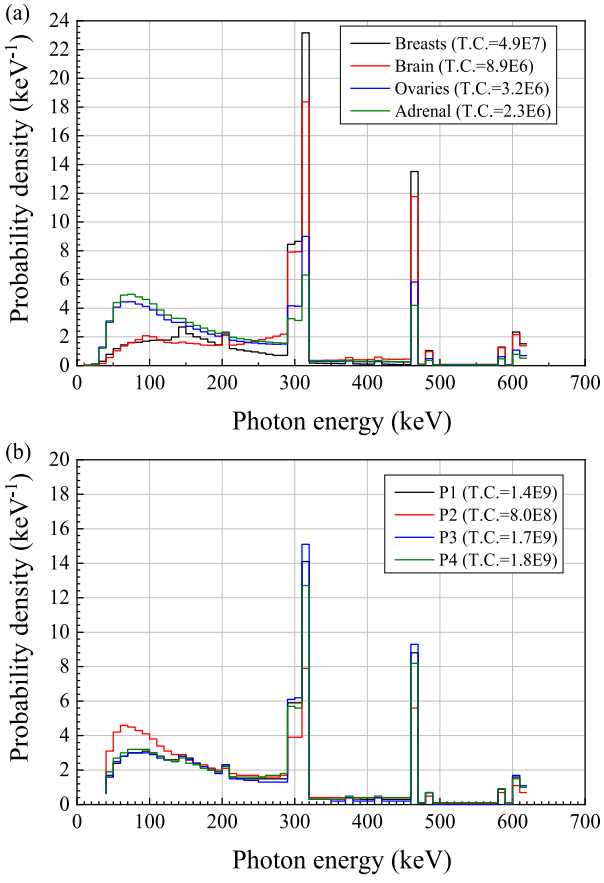

Fig. A1. Photon probability density distribution for (a) the organs within P1 and (b) the arithmetic means over all organ fluences in each phantom. The total counts (T.C.) of the incident photons are given in the legend.

Table A1
Work-flow table of the comparison between the experimental part to the computational part showing the corresponding dose values. 'O' indicates that the participant has submitted results.

Experimental part					Computational part				
Phantom	Item	Used dosimeters	Measuring institutes	References	G(Lab1) (Lab1 using Geant4)	M(Lab2) (Lab2 using MCNP6.2)	M(Lab3) (Lab3 using MCNP6.2)	G(Lab4) (Lab4 using Geant4)	M(Lab4) (Lab4 using MCNP6.2)

(*continued on next page*)

Table A1 (*continued*)

Experimental part					Computational part				
Phantom	Item	Used dosimeters	Measuring institutes	References	G(Lab1) (Lab1 using Geant4)	M(Lab2) (Lab2 using MCNP6.2)	M(Lab3) (Lab3 using MCNP6.2)	G(Lab4) (Lab4 using Geant4)	M(Lab4) (Lab4 using MCNP6.2)
P1	Organs	RPLD	IRSN	Waldner et al. (2021)	O (Intact mesh phantoms)	O (Torso voxel phantom)	O (Torso voxel phantom)	O (Intact mesh phantoms)	O (Intact voxel phantom)
P2		TLD (MCP-N)	SCK-CEN			-(Rect. Water slab)			
P3		–	–			–			
P4		OSLD (NaCl)	Lund univ.			–			
All	Surface dosimeters	RPLD	IRSN		O	–	–	–	–
		OSLD (NaCl)	Lund univ.		O	–	–	–	
	Mobile phones	LUXEL	OSU	(Woda et al, in preparation)	O	O (Only P1)	O	–	–
		Glass	HMGU		O	O (Only P1)	O	–	–
		TLD (GR-200)	IRSN		O	O (Only P1)	O	–	–
	Vacuum flasks	RPLD	IRSN	Endesfelder et al. (2021)	O	–	O (w/o flask)	–	–
	Extra materials	RPLD	IRSN	In preparation	O	–	–	–	–

Table A2
Absorbed dose in teeth of the four computerized phantoms estimated by MCNP6.2

	P1	P2	P3	P4
Teeth dose (Gy)	0.33	0.06	0.23	0.24

Table A3
The calculated whole-body doses from different laboratories. The effective dose is given in the bracket. (*simulated without limbs) (Unit: Gy)

	P1	P2	P3	P4
G(Lab1)	0.53 (0.61)	0.09 (0.08)	0.21 (0.24)	0.38 (0.39)
G(Lab4)	0.54 (0.62)	0.09 (0.08)	0.21 (0.25)	0.38 (0.39)
M(Lab2*)	0.41 (0.62)			
M(Lab3*)	0.41 (0.62)	0.07 (0.11)	0.13 (0.21)	0.30 (0.40)
M(Lab4)	0.53 (0.61)	0.11 (0.10)	0.21 (0.24)	0.37 (0.38)

Table A4
Comparison of the RPLD doses attached to the extra materials estimated from the Geant4 simulation and measurements. Relative differences of the calculation to the measurement are given in the right column. (Dose unit: Gy)

Phantom	ID	Geant4	Meas.	Relative difference
P1	Ex-71	0.83	0.80	5%
	Ex-65	1.24	1.18	6%
	Ex-68	1.49	1.68	−11%
	Ex-66	1.99	2.04	−2%
	Ex-207	2.17	1.82	19%
	Ex-61	2.10	1.52	39%
	Ex-80	0.39	0.24	61%
	Ex-164	0.63	0.47	33%
	Ex-78	0.78	0.67	16%
	Ex-70	1.70	1.92	−11%
	Ex-833	1.92		
	Ex-206	2.10	1.52	39%
	Ex-74	0.05	0.04	30%
P2	Ex-72	0.11	0.18	−41%
	Ex-69	0.18	0.31	−41%
	Ex-67	0.15	0.37	−58%
	Ex-836	0.17	0.37	−53%

(*continued on next page*)

Table A4 (*continued*)

Phantom	ID	Geant4	Meas.	Relative difference
	Ex-79	0.07	0.06	23%
P3	Ex-168	0.13	0.13	3%
	Ex-839	0.34	0.29	19%
	Ex-180	0.30	0.32	−6%
P4	Ex-838	0.74	0.67	10%
	Ex-63	1.34	1.02	32%
	Ex-64	1.43	1.13	26%
	Ex-835	1.50	1.21	24%
	Ex-837	1.37	1.14	20%
	Ex-840	1.18	1.06	11%

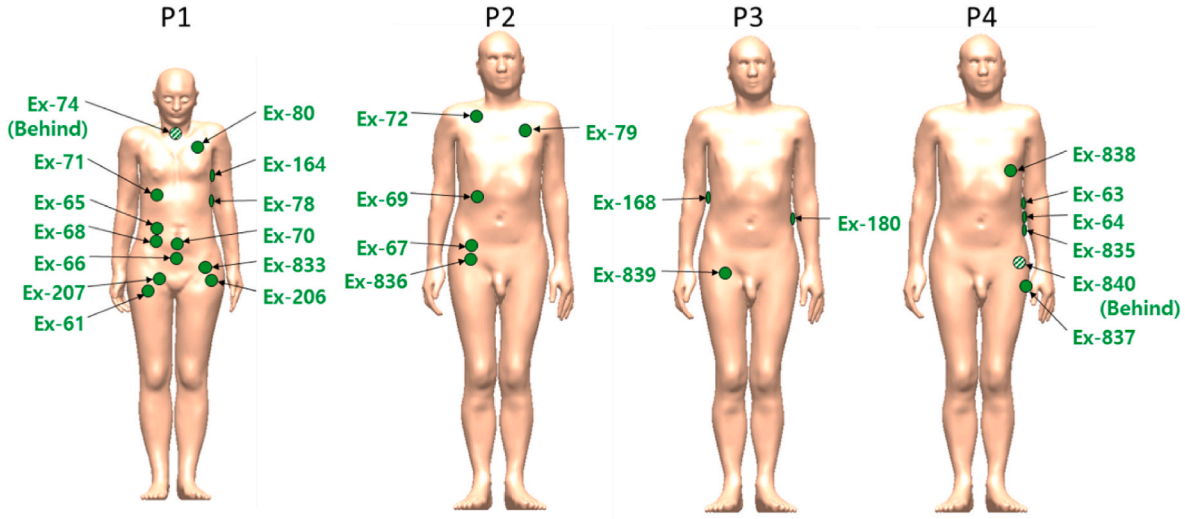

Fig. A2. The locations of RPLDs for extra materials in Geant4 simulation.

Data availability

Data will be made available on request.

References

Abend, M., Amundson, S., Badie, C., Brzoska, K., Hargitai, R., Kriehuber, R., Schüle, S., Kis, E., Ghandhi, S., Lumniczky, K., 2021. Inter-laboratory comparison of gene expression biodosimetry for protracted radiation exposures as part of the RENEB and EURADOS WG10 2019 exercise. Sci. Rep. 11, 1–15.

Agostinelli, S., Allison, J., Amako, K.a., Apostolakis, J., Araujo, H., Arce, P., Asai, M., Axen, D., Banerjee, S., Barrand, G., 2003. GEANT4—a simulation toolkit. Nucl. Instrum. Methods Phys. Res. Sect. A Accel. Spectrom. Detect. Assoc. Equip. 506, 250–303.

Ainsbury, E., Badie, C., Barnard, S., Manning, G., Moquet, J., Abend, M., Antunes, A.C., Barrios, L., Bassinet, C., Beinke, C., Bortolin, E., Bossin, L., Bricknell, C., Brzoska, K., Buraczewska, I., Castano, C.H., Cemusova, Z., Christiansson, M., Cordero, S.M., Cosler, G., Monaca, S.D., Desangles, F., Discher, M., Dominguez, I., Doucha-Senf, S., Eakins, J., Fattibene, P., Filippi, S., Frenzel, M., Georgieva, D., Gregoire, E., Guogyte, K., Hadjidekova, V., Hadjiiska, L., Hristova, R., Karakosta, M., Kis, E., Kriehuber, R., Lee, J., Lloyd, D., Lumniczky, K., Lyng, F., Macaeva, E., Majewski, M., Vanda Martins, S., McKeever, S.W., Meade, A., Medipally, D., Meschini, R., M'Kacher, R., Gil, O.M., Montero, A., Moreno, M., Noditi, M., Oestreicher, U., Oskamp, D., Palitti, F., Palma, V., Pantelias, G., Pateux, J., Patrono, C., Pepe, G., Port, M., Prieto, M.J., Quattrini, M.C., Quintens, R., Ricoul, M., Roy, L., Sabatier, L., Sebastia, N., Sholom, S., Sommer, S., Staynova, A., Strunz, S., Terzoudi, G., Testa, A., Trompier, F., Valente, M., Hoey, O.V., Veronese, I., Wojcik, A., Woda, C., 2017. Integration of new biological and physical retrospective dosimetry methods into EU emergency response plans - joint RENEB and EURADOS inter-laboratory comparisons. Int. J. Radiat. Biol. 93, 99–109.

Ainsbury, E., Bakhanova, E., Barquinero, J., Brai, M., Chumak, V., Correcher, V., Darroudi, F., Fattibene, P., Gruel, G., Guclu, I., 2011. Review of retrospective dosimetry techniques for external ionising radiation exposures. Radiat. Protect. Dosim. 147, 573–592.

Bailiff, I.K., Sholom, S., McKeever, S.W.S., 2016. Retrospective and emergency dosimetry in response to radiological incidents and nuclear mass-casualty events: a review. Radiat. Meas. 94, 83–139.

Bassinet, C., Woda, C., Bortolin, E., Della Monaca, S., Fattibene, P., Quattrini, M.C., Bulanek, B., Ekendahl, D., Burbidge, C.I., Cauwels, V., Kouroukla, E., Geber-Bergstrand, T., Mrozik, A., Marczewska, B., Bilski, P., Sholom, S., McKeever, S.W.S., Smith, R.W., Veronese, I., Galli, A., Panzeri, L., Martini, M., 2014. Retrospective radiation dosimetry using OSL of electronic components: results of an inter-laboratory comparison. Radiat. Meas. 71, 475–479.

Benali, A.-H., Ishak-Boushaki, G.M., 2018. Energy response of FD-7 RPL glass dosimeter compared with LiF Mg, Ti and Al2003: C dosimeters. J. Instrum. 13, P11015.

Benali, A.H., Ishak-Boushaki, G.M., Nourreddine, A.M., Allab, M., Papadimitroulas, P., 2017. A comparative evaluation of luminescence detectors: RPL-GD-301, TLD-100 and OSL-AL2O3:C, using Monte Carlo simulations. J. Instrum. 12, P07017. P07017.

CIRS, 2021. ATOM® dosimetry verification phantoms. https://www.cirsinc.com/products/radiation-therapy/atom-dosimetry-verification-phantoms/. (Accessed 29 September 2021).

Cunningham, J.R., Schulz, R.J., 1984. On the selection of stopping-power and mass energy-absorption coefficient ratios for high-energy x-ray dosimetry. Med. Phys. 11, 618–623.

Discher, M., Eakins, J., Woda, C., Tanner, R., 2021a. Translation of the absorbed dose in the mobile phone to organ doses of an ICRP voxel phantom using MCNPX simulation of an Ir-192 point source. Radiat. Meas. 146, 106603.

Discher, M., Greiter, M., Woda, C., 2014. Photon energy dependence and angular response of glass display used in mobile phones for accident dosimetry. Radiat. Meas. 71, 471–474.

Discher, M., Woda, C., 2013. Thermoluminescence of glass display from mobile phones for retrospective and accident dosimetry. Radiat. Meas. 53–54, 12–21.

Discher, M., Woda, C., Ekendahl, D., Rojas-Palma, C., Steinhäusler, F., 2021b. Evaluation of physical retrospective dosimetry methods in a realistic accident scenario: results of a field test. Radiat. Meas. 142, 106544.

Eakins, J., Discher, M., Kim, H., Kim, M.C., Lee, H., Lee, J., Van Hoey, O., Yu, H., Ainsbury, E., Bassinet, C., 2024. Dose conversion in retrospective dosimetry: results and implications from an inter-laboratory comparison featuring a realistic exposure scenario. Radiat. Meas. 179, 107307.

Eakins, J.S., Kouroukla, E., 2015. Luminescence-based retrospective dosimetry using Al2O3 from mobile phones: a simulation approach to determine the effects of position. J. Radiol. Prot. 35, 343–381.

Endesfelder, D., Oestreicher, U., Kulka, U., Ainsbury, E.A., Moquet, J., Barnard, S., Gregoire, E., Martinez, J.S., Trompier, F., Ristic, Y., 2021. RENEB/EURADOS field exercise 2019: robust dose estimation under outdoor conditions based on the dicentric chromosome assay. Int. J. Radiat. Biol. 97, 1181–1198.

Entine, F., Garnier, G., Dondey, M., Rizzi, Y., Gobert, A., Bassinet, C., Papin, S., Pennacino, I., Cazoulat, A., Amabile, J., 2022. SEED: an operational numerical tool for dosimetric reconstruction in case of external radiological overexposure. Health Phys. 122, 271–290.

Furhang, E.E., Chui, C.S., Lovelock, M., 1995. Mean mass energy absorption coefficient ratios for megavoltage x-ray beams. Med. Phys. 22, 525–530.

Gasparian, P., Vanhavere, F., Yukihara, E., 2012. Evaluating the influence of experimental conditions on the photon energy response of Al2O3:C optically stimulated luminescence detectors. Radiat. Meas. 47, 243–249.

Gregoire, E., Hadjidekova, V., Hristova, R., Gruel, G., Roch-Lefevre, S., Voisin, P., Staynova, A., Deleva, S., Ainsbury, E.A., Lloyd, D.C., Barquinero, J.F., 2013. Biological dosimetry assessments of a serious radiation accident in Bulgaria in 2011. Radiat. Protect. Dosim. 155, 418–422.

Hranitzky, C., Stadtmann, H., Olko, P., 2006. Determination of LiF: Mg, Ti and LiF: Mg, Cu, P TL efficiency for X-rays and their application to Monte Carlo simulations of dosemeter response. Radiat. Protect. Dosim. 119, 483–486.

Hubbell, J., Seltzer, S., 2004. NIST standard reference database 126, tables of X-ray mass attenuation coefficients and mass energy-absorption coefficients from 1 keV to 20 MeV for elements Z= 1 to 92 and 48 additional substances of dosimetric interest. Gaithersburg, MD: NIST Standard Reference Database 126.

Huet, C., Trompier, F., Clairand, I., Queinnec, F., Bottollier-Depois, J.F., 2008. Physical dosimetric reconstruction of a radiological accident at Fleurus (Belgium) on 11 March 2006. Radiat. Meas. 43, 845–848.

Hurtado, J.L., Lee, C., Lodwick, D., Goede, T., Williams, J.L., Bolch, W.E., 2012. Hybrid computational phantoms representing the reference adult male and adult female: construction and applications for retrospective dosimetry. Health Phys. 102, 292–304.

IAEA, 2004. The Radiological Accident in Cochabamba. INTERNATIONAL ATOMIC ENERGY AGENCY, Vienna.

IAEA, 2006. Environmental Consequences of the Chernobyl Accident and Their Remediation: Twenty Years of Experience. INTERNATIONAL ATOMIC ENERGY AGENCY, Vienna.

IAEA, 2015. The Fukushima Daiichi Accident. INTERNATIONAL ATOMIC ENERGY AGENCY, Vienna.

IAEA, 2018. The Radiological Accident in Chilca. INTERNATIONAL ATOMIC ENERGY AGENCY, Vienna.

IAEA, 2019. The Radiological Accident in Ventanilla. INTERNATIONAL ATOMIC ENERGY AGENCY, VIENNA.

IAEA, 2024. Accident reports. https://www.iaea.org/publications/search/topics/accident-reports. (Accessed 24 June 2024).

ICRP, 2007. ICRP publication 103: the 2007 recommendations of the international commission on radiological protection. INTERNATIONAL COMMISSION ON RADIOLOGICAL PROTECTION.

ICRP, 2008. ICRP Publication 107: nuclear decay data for dosimetric calculations. INTERNATIONAL COMMISSION ON RADIOLOGICAL PROTECTION.

ICRP, 2009. ICRP Publication 110 : the ICRP reference computational phantoms for the adult male and female. INTERNATIONAL COMMISSION ON RADIOLOGICAL PROTECTION.

ICRP, 2020. ICRP Publication 145 : adult mesh-type reference computational phantoms. INTERNATIONAL COMMISSION ON RADIOLOGICAL PROTECTION.

Ixquiac-Cabrera, J., Brandan, M., Martínez-Dávalos, A., Rodríguez-Villafuerte, M., Ruiz-Trejo, C., Gamboa-deBuen, I., 2011. Effect of spectral shape in the relative efficiency of LiF: Mg, Ti exposed to 20 keV effective energy X-rays. Radiat. Meas. 46, 389–395.

Kim, H., Kim, M.C., Lee, J., Chang, I., Lee, S.K., Kim, J.-L., 2019a. Thermoluminescence of AMOLED substrate glasses in recent mobile phones for retrospective dosimetry. Radiat. Meas. 122, 53–56.

Kim, H., Yu, H., Discher, M., Kim, M.C., Choi, Y., Lee, H., Lee, J.T., Lee, H., Kim, Y.-s., Kim, H.S., Lee, J., 2022. A small-scale realistic inter-laboratory accident dosimetry comparison using the TL/OSL from mobile phone components. Radiat. Meas. 150, 106696.

Kim, M.C., Kim, H., Han, H., Lee, J., Lee, S.K., Chang, I., Kim, J.-L., Kim, C.H., 2019b. A study on dose conversion from a material to human body using mesh phantom for retrospective dosimetry. Radiat. Meas. 126, 106126.

Kim, M.C., Kim, H., Han, H., Lee, J., Lee, S.K., Chang, I., Kim, J.-L., Kim, C.H., 2019c. A study on dose conversion from a material to human body using mesh phantom for retrospective dosimetry. Radiat. Meas. 126.

Kouroukla, E., Bailiff, I., Terry, I., Bowen, L., 2014. Luminescence characterisation of alumina substrates using cathodoluminescence microscopy and spectroscopy. Radiat. Meas. 71, 117–121.

Kulka, U., Abend, M., Ainsbury, E., Badie, C., Barquinero, J.F., Barrios, L., Beinke, C., Bortolin, E., Cucu, A., De Amicis, A., 2017. RENEB–Running the European Network of biological dosimetry and physical retrospective dosimetry. Int. J. Radiat. Biol. 93, 2–14.

Kulka, U., Wojcik, A., Di Giorgio, M., Wilkins, R., Suto, Y., Jang, S., Quing-Jie, L., Jiaxiang, L., Ainsbury, E., Woda, C., 2018. Biodosimetry and biodosimetry networks for managing radiation emergency. Radiat. Protect. Dosim. 182, 128–138.

Kurihara, O., Ha, W.-H., Qinjian, C., Jang, S., 2020. ARADOS: Asian network for radiation dosimetry. Radiat. Meas., 106336

Lataillade, J., Doucet, C., Bey, E., Carsin, H., Huet, C., Clairand, I., Bottollier-Depois, J., Chapel, A., Ernou, I., Gourven, M., 2007. New approach to radiation burn treatment by dosimetry-guided surgery combined with autologous mesenchymal stem cell therapy. Regen. Med. 2, 785–794.

Lemosquet, A., Clairand, I., De Carlan, L., Franck, D., Aubineau-Laniece, I., Bottollier-Depois, J.-F., 2004. A computational tool based on voxel geometry for dose reconstruction of a radiological accident due to external exposure. Radiat. Protect. Dosim. 110, 449–454.

Musolino, S.V., 2001. Absorbed Dose Determination in External Beam Radiotherapy: an International Code of Practice for Dosimetry Based on Standards of Absorbed Dose to Water; Technical Reports Series No. 398. LWW.

Parisi, A., Dabin, J., Schoonjans, W., Van Hoey, O., Mégret, P., Vanhavere, F., 2019. Photon energy response of LiF: Mg, Ti (MTS) and LiF: Mg, Cu, P (MCP) thermoluminescent detectors: experimental measurements and microdosimetric modeling. Radiat. Phys. Chem. 163, 67–73.

Reyes, E.H., Baciu, F., Benderitter, M., Lataillade, J.J., Bey, E., Trompier, F., Tamarat, R., 2016. Medical response to radiological accidents in Latin America and international assistance. Radiat. Res. 185, 359–365.

Rojas-Palma, C., Woda, C., Discher, M., Steinhäusler, F., 2020. On the use of retrospective dosimetry to assist in the radiological triage of mass casualties exposed to ionising radiation. J. Radiol. Prot. 40, 1286.

RSD, 2021. The Alderson radiation therapy phantom. https://rsdphantoms.com/radiation-therapy/the-alderson-radiation-therapy-phantom/. (Accessed 29 September 2021).

Sholom, S., McKeever, S.W.S., 2017. Developments for emergency dosimetry using components of mobile phones. Radiat. Meas. 106, 416–422.

Trompier, F., Queinnec, F., Bey, E., De Revel, T., Lataillade, J.J., Clairand, I., Benderitter, M., Bottollier-Depois, J.F., 2014. EPR retrospective dosimetry with fingernails: report on first application cases. Health Phys. 106, 798–805.

Waldner, L., Bernhardsson, C., Woda, C., Trompier, F., Van Hoey, O., Kulka, U., Oestreicher, U., Bassinet, C., Rääf, C., Discher, M., 2021. The 2019–2020 EURADOS WG10 and RENEB field test of retrospective dosimetry methods in a small-scale incident involving ionizing radiation. Radiat. Res. 195, 253–264.

Waldner, L., Rääf, C., Hinrichsen, Y., Herrnsdorf, L., Bernhardsson, C., 2020. Experimentally determined and Monte Carlo–calculated energy dependence of NaCl pellets read by optically stimulated luminescence for photon beams in the energy range 30 keV to 1.25 MeV. J. Radiol. Prot. 40, 1321.

Weihai, Z., Weiqi, L., Gang, H., Guoying, Z., Guocai, M., 2007. Comparisons of dosimetric properties between GD-300 series of radiophotoluminescent glass detectors and GR-200 series of thermoluminescent detectors. Nucl. Sci. Tech. 18, 362–365.

Werner, C.J., Bull, J., Solomon, C., Brown, F., McKinney, G., Rising, M., Dixon, D., Martz, R., Hughes, H., Cox, L., 2018. MCNP6. 2 Release Notes. Los Alamos National Laboratory report LA-UR-18-20808.

Williams, B.B., Flood, A.B., Salikhov, I., Kobayashi, K., Dong, R., Rychert, K., Du, G., Schreiber, W., Swartz, H.M., 2014. In vivo EPR tooth dosimetry for triage after a radiation event involving large populations. Radiat. Environ. Biophys. 53, 335–346.

Woda, C., Bassinet, C., Waldner, L., Bernhardsson, C., Trompier, F., Discher, M., Hoey, O. V., Eakins, J.S., Kim, H., Lee, J., Kim, M.C., Yu, H., Sholom, S., McKeever, S.W.S., Bossin, L., Bailiff, I., Mrozik, A., Cemusova, Z., Ekendahl, D., Bortolin, E., Monaca, S. D., Fattibene, P., Veronese, I., Ainsbury, E., in preparation. The 2019–2020 EURADOS WG10 and RENEB Field Test of a Small-Scale Incident Involving Ionizing Radiation: Results of Physical Retrospective Dosimetry Using Components of Mobile Phones.

Yeom, Y.S., Han, M.C., Choi, C., Han, H., Shin, B., Furuta, T., Kim, C.H., 2019. Computation speeds and memory requirements of mesh-type ICRP reference computational phantoms in Geant4, MCNP6, and PHITS. Health Phys. 116, 664–676.